Acta Pharmaceutica Sinica B 2025;15(9):4844–4871

Chinese Pharmaceutical Association
Institute of Materia Medica, Chinese Academy of Medical Sciences

Acta Pharmaceutica Sinica B

www.elsevier.com/locate/apsb
www.sciencedirect.com

ORIGINAL ARTICLE

Discovery of powerful multifaceted antioxidant for combating oxidative stress associated with neurodegenerative disorders

Juhee khan[a,b], Prabir kumar Gharai[a,b], Shubham Garg[b], Sanju Gupta[b], Mohammad Umar Arshi[b], Rathnam Mallesh[a,b,c], Surajit Ghosh[a,b,c,*]

[a]*Organic and Medicinal Chemistry and Structural Biology and Bioinformatics Division, CSIR-Indian Institute of Chemical Biology, Kolkata 700032, India*
[b]*Department of Bioscience and Bioengineering, Indian Institute of Technology, Rajasthan 342037, India*
[c]*National Institute of Pharmaceutical Education and Research, Kolkata 700054, India*

Received 9 August 2024; received in revised form 16 April 2025; accepted 24 April 2025

KEY WORDS

Neuroprotection;
Oxidative stress;
Polyphenol;
Nrf2/ARE pathway;
Ischemic stroke;
tBCCAO;
Antioxidant;
Hydrogen peroxide

Abstract Amidst the tangled web of neurons, antioxidants stand as silent sentinels, shielding the delicate threads from the raging storm of oxidative stress in the realm of neurological affliction. Herein, we showcased an innovative design strategy to develop a novel powerful antioxidant small molecule (AOX), designed with the synergistic integration of EGCG (epigallocatechin gallate), gallic acid, and coupled with the metal-chelating capabilities of 8-hydroxy quinoline functional moieties that exhibit multifunctional activity in combating oxidative stress *via* activating the anti-oxidative, anti-apoptotic and anti-inflammatory activity, showcasing the potential for a transformative impact in neuroprotection from oxidative insults. Our work addresses oxidative stress in neuronal systems by providing a thorough examination of oxidative stress caused by hydrogen peroxide in PC12 cell line-derived neurons by shedding light on the antioxidative mechanisms orchestrated by our novel small molecule. Particularly our designed molecule (AOX) provides neuroprotection by mitigating mitochondrial impairment and activating the Nrf2/ARE (nuclear factor erythroid 2-related factor 2/antioxidant response element) pathway and it also demonstrates remarkable resilience against neuroinflammation, as evidenced by minimal alterations in neuroinflammatory markers such as GFAP, IBA1, and S100β in a transient bilateral common carotid artery occlusion (tBCCAO) ischemic stroke model.

*Corresponding author.
E-mail address: sghosh@iitj.ac.in (Surajit Ghosh).

Peer review under the responsibility of Chinese Pharmaceutical Association and Institute of Materia Medica, Chinese Academy of Medical Sciences.

https://doi.org/10.1016/j.apsb.2025.04.024

1. Introduction

A major and expanding global health concern is neurodegenerative disorders (NDDs), which are predominantly defined by the progressive loss of neuronal structure and function in specific regions of the brain. Prominent examples of such disorders encompass Alzheimer's disease (AD), Parkinson's disease (PD), Huntington's disease (HD), Multiple Sclerosis (MS), and Amyotrophic Lateral Sclerosis (ALS) impacting millions of people globally and causing significant financial and psychological hardships. Despite the existence of numerous approved medications for addressing NDDs, the majority merely alleviate associated symptoms and do not possess the ability to reverse the complications[1]. The exact cause of most NDDs is largely unclear, stemming from multifactorial origins. Increasing evidence suggests that the progression of neuron and glial degeneration involves oxidative damage, mitochondrial dysfunction, and disruption of calcium homeostasis. However, the link between oxidative stress and the advancement of several NDDs arises from an imbalance in pro-oxidant/antioxidant equilibrium, resulting in the production of harmful reactive oxygen species (ROS) for neurons and glial cells[2,3]. A healthy cell is defined by a balance between the generation of ROS (superoxide, hydrogen peroxide, hydroxyl radical, hydroxyl ion, and nitric oxide) and the capacity to remove them. Thus, a need for the removal of ROS by antioxidants has a significant impact on controlling cell signalling and function. The capacity of each of these ROS to harm cellular components is determined by their chemical reactivity and the location of synthesis inside the cell[4,5]. Mitochondria are the primary cellular contributors of ROS, producing superoxide radicals and hydrogen peroxide during oxygen consumption. Various sites within the mitochondrial electron transport chain, such as NADH-ubiquinone oxidoreductase in complex I, the coenzyme Q pool, and complexes II and III, contribute to superoxide production[6]. In addition to their distinct disease characteristics, NDDs exhibit various shared pathophysiological mechanisms, including those influenced by inflammation, immune exhaustion, and compromise of the neurovascular unit, akin to stroke. The presence of stroke often coincides with several NDDs, including AD, PD, and MS, thereby heightening the risk of neurodegeneration[7]. This leads to mechanisms such as increased H_2O_2 release that cause oxidative damage and neuronal cell death[8].

Chemical species known as free radicals are defined by their reactive nature and the presence of an unpaired electron in their outer orbit. Simultaneously, they also exhibit the ability to exist independently. ROS are oxygenated molecules that are both free radical and non-free radical, such as hydroxyl radical (·OH), singlet oxygen (1/2 O_2), superoxide ($O_2^{\cdot-}$), and hydrogen peroxide (H_2O_2)[9]. These reactive species contribute to oxidative stress and redox imbalance. Their generation is inherent in metabolic processes and exposure to environmental oxidants, including microbial infections, physical activity, and pollutants. Free radical damage in oxidative stress has been shown to have a role in the pathogenesis and pathophysiology of many chronic health conditions, including NDDs[10]. Briefly, ROS from subcellular organelles can target biomolecules and pathways, leading to neuronal dysfunction and associated NDDs. For instance, ROS like ·HO and $O_2^{\cdot-}$ catalyse lipid peroxidation, while highly reactive molecules like ·OH and $O_2^{\cdot-}$ induce DNA damage and impact the DNA damage response (DDR). Moreover, these ROS can damage proteins, disrupting covalent bonds, and thereby destabilizing them[11]. Fortunately, our body possesses a defence system against these harmful molecules and ions known as antioxidants. The antioxidant defence system comprises enzymes like superoxide dismutase, and catalase, and non-enzymatic antioxidants such as glutathione, vitamin E, and vitamin C, which work synergistically to protect cells from the damaging effects of free radicals and ROS. In addition, high concentrations of transition metals such as copper (Cu), iron (Fe), and Zinc (Zn) in the brain are essential for cellular processes, metalloenzyme activity and synaptic neuronal activity[12]. It is widely acknowledged that metal imbalance plays a major role in the development of numerous neurodegenerative illnesses, including PD, AD, and MS[13]. Increased concentrations of redox-reactive metal ions, such Cu and Fe, in the brain, can instigate the generation of ROS, resulting in lipid peroxidation and the formation of toxic reactive aldehyde products (malondialdehyde and 4-hydroxy-2-nonenal, 4-HNE)[14]. These elevated redox-reactive metal ions in the brain induce cellular damage and neuronal toxicity, disrupting proteasomal protein degradation and promoting misfolding, thereby resisting degradation. Misfolded proteins aggregate and accumulate as a result of the interaction between metal and proteins, across various brain regions, resulting in neurotoxicity, neuronal dysfunction, and cell death[15]. This suggests that dysregulation of metal homeostasis, along with ROS generation and metal ion−protein interactions, contributes to the pathogenesis of neurodegenerative diseases[16−19]. Consequently, therapeutic agents with multi-targeting properties, encompassing metal chelation, antioxidant, and neuroprotective effects, hold promise for restoring metal balance and reducing neurotoxicity in neurodegenerative diseases.

In summary, the emergence of AOX marks a significant breakthrough in therapeutic intervention, poised to revolutionize the landscape of neuroprotection by offering a formidable defence against metal and ROS-induced neurotoxicity. With its unparalleled ability to rejuvenate neurons, regulate metal homeostasis, and mitigate oxidative stress, AOX holds immense promise for preserving neuronal integrity and fostering sustained well-being in individuals afflicted by neurodegenerative disorders. Additionally, AOX has shown promising results demonstrated by its encouraging outcomes in *in vivo* experiments conducted in the tBCCAO model of ischemic stroke. Its multifaceted approach makes it a promising molecule in combating the detrimental effects on neuronal health both *in vivo* and *in vitro* model.

2. Results and discussion

2.1. Design strategy, synthesis, and characterization of AOX

Our design strategy is based on the metal chelation, antioxidant, and enhancement of neuronal outgrowth to recover the neurons

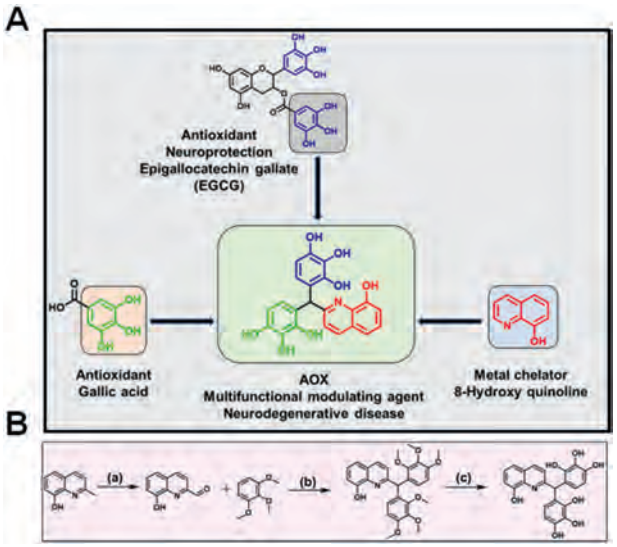

Scheme 1 Design strategy and synthesis of AOX. (A) Multifunctional agent AOX was designed by integrating 8-hydroxy quinoline as a potent metal chelator and polyhydroxy phenols for antioxidant activity. (B) Synthesis scheme of AOX(a) SeO_2, 1,4-dioxane, H_2O, reflux at 110 °C for 12 h. (b) Polyphosphoric acid. (c) BBr_3, dichloromethane, −78 °C.

from oxidative stress mediated neurodegenerative diseases (Scheme 1A). According to our rational design, the development of antioxidant multifunctional agent (AOX) is based on majorly four important aspects. First, due to its multifunctional qualities, including a range of bioactivities and therapeutic potential, the hydroxyquinoline derivative 8-hydroxy quinoline (8HQ) is the most intriguing moiety to be investigated[20]. Among seven isomeric monohydroxy quinolines, 8HQ is the only one able to use chelation to create compounds with divalent metal ions. Consequently, we employed 8HQ as a strong chelator that might help to restore metal balance and be helpful in treating neurological illnesses linked to metal imbalance. Second, polyhydroxy phenolic compound gallic acid (GA) and its derivatives have a remarkable neuroprotection against oxidative damage caused by ROS[21]. The studies indicate that gallic acid is effective against a wide range of diseases like cardiovascular diseases[22−24], liver diseases[25], inflammation[26], and neurodegenerative diseases[27,28]. Third, the benefits of polyphenols, especially their active component EGCG, have drawn significant interest in them as a possible therapeutic agent for avoiding cancer, inflammatory diseases, and neurological disorders[29,30]. Their anti-inflammatory, anti-carcinogenic, anti-apoptotic, antioxidant, and radical scavenging qualities are primarily responsible for this capacity. It has been demonstrated that EGCG exhibits potential effects in the PD, including the attenuation of apoptosis, the suppression of ROS and free intracellular calcium build up, the modification of signalling pathways, and the reduction of nitric oxide levels and ROS[31]. While in the case of AD, it has been seen that there is a suppression of tau protein phosphorylation, a reduction in the synthesis of beta-amyloid, a promotion of beta-amyloid breakdown, a decrease in beta and gamma secretase activity, and a higher level of alpha secretase activity[32]. Fourth and most importantly, neurite loss is one of the major and serious characteristic features of neuronal injury. In addition to neuroprotection, normal physiological functioning in the wounded brain must be restored by reorganizing the lost neural network. It has been proposed that brain function recovery requires the regeneration of the neuronal and synaptic networks in the injured brain[33]. Although the central nervous system's (CNS) irreversible nerve regeneration process, it has recently been shown that damaged neurons can actively recover when stimulatory chemicals like nerve growth factor (NGF) and brain-derived neurotrophic factor are present (BDNF)[33−35]. Furthermore, additional data suggests that substances able to improve neurotrophic factors' ability to promote neurite outgrowth may be helpful in the treatment of neurological conditions including Parkinson's disease and Alzheimer's disease. According to a recent study, in PC12 cells, EGCG by itself enhanced NGF-induced neurite outgrowth[36]. Nobiletin flavonoid has shown neurite outgrowth in PC12-derived cells[37]. For this, we incorporated the polyhydroxy phenols in the AOX to adopt the antioxidant property along with neuronal outgrowth capability to recover and restore the neuronal function in the brain. We anticipated that these multifunctional therapeutic agent AOX would inherit the antioxidant, neuronal outgrowth, and neuroprotective properties of polyphenols from one end and the potential to modulate protein aggregation and metal chelation from the other end. Thus, the molecule AOX is expected to regulate metal homeostasis, metal, and ROS inducing toxicity and prevent neuronal death from ROS. The multifunctional AOX was synthesized (Scheme 1B) through a three-step reaction. In the first step, 8-hydroxyquinoline-2-carbaldehyde (Intermediate-1) was synthesized from 2-methylquinolin-8-ol using SeO_2. In the second step, 2-(bis(2,3,4-trimethoxyphenyl) methyl) quinolin-8-ol (Intermediate-2) was synthesized by using polyphosphoric acid and the mechanism of this coupling reaction of 8-hydroxyquinoline-2-carbaldehyde and trimethoxybenzene are shown in Supporting Information Fig. S1. In this mechanism, the initial reaction of a suitable electron-rich species, trimethoxybenzene (A1), with carbonyl substrate (Intermediate-1), stimulated through protonation by polyphosphoric acid (A2), results in the formation of the adduct D from the previously produced B and C. Simultaneous nucleophilic C-2 reaction by A1 results in the intermediate F, which following deprotonation provides product Intermediate-2 through previous literature as cited that aldehyde coupling with phenolic compounds yields *para*-substituted products under acidic conditions[38,39]. However, this study differs in its choice of starting material, employing 1,2,3-trimethoxybenzene, and the mechanism diverges from that of phenolic compounds. Here, the methoxy group with less hindered side participates in electron donation, resulting in different product formation, as confirmed by ^{1}H NMR analysis. Furthermore, have proposed that nanoparticle-modified polyphosphoric acid facilitates aldehyde-trimethoxybenzene coupling[40]. The plausible mechanism of Intermediate-2 (Fig. S1 in ESI) elucidates the compound's formation. Finally, the product AOX was synthesized by using BBr_3 to Intermediate-2. The reagent BBr_3 cleaves the O−C bond of the $-OCH_3$ group to produce the −OH group. The AOX was purified by column chromatography and characterized by ^{1}H NMR, ^{13}C NMR, and HRMS spectra. The purity of this AOX was measured by using HPLC analysis and the spectra show that AOX is 99.54% pure (Fig. S2−S11).

2.2. *Metal ion chelation*

Through a prolonged redox cycling method, coordination of the redox−active transition metal ion (Cu^{2+}) with amyloid beta ($A\beta$) has been demonstrated to promote the stabilization of

oligomerization and fibrilization, and the production of excessive ROS[41]. Key tactics to lessen the burden of comprehensive Aβ toxicity, including oxidative stress, include efficient chelation and sequestration of redox−active transition metal ions from Aβ metal complexes and subsequently reducing excessive ROS[42,43]. As the Cu^{2+} ion has the crucial role of ROS generation through binding with Aβ, so we were interested to check the Cu^{2+} ion sequestration from the Aβ−Cu^{2+} complex. Before this, the chelation capability of AOX with Cu^{2+} ion including different biologically active transition metal ions was studied by UV absorption measurement. The absorption maximum of AOX shifted from 245 to 263 nm in the presence of Cu^{2+} ion. Similarly, we also checked the chelation of other biological metal ions and the result revealed significant chelation except for Co^{2+} and Mg^{2+} (Absorption maxima; λ_{max}: Zn^{2+}; 259 nm, Fe^{3+}; 257 nm, Al^{3+}; 262 nm, Ni^{2+}; 263 nm) (Supporting Information Fig. S12). Next, Cu^{2+} ion titration with the ligand AOX was carried out by absorption spectroscopy study to know the binding stoichiometry. The ratio of Cu^{2+} ion has taken 0.25 to 3.5 equivalent compared with ligand AOX (10 μmol/L). The titration curve shows that AOX chelates the Cu^{2+} ion with 1:1 binding stoichiometry (Supporting Information Fig. S13). Finally, we performed a tyrosine quenching assay as tyrosine (^{10}Tyr) residue's intrinsic fluorescence in Aβ_{42} peptide (λ_{ex}: 285 nm and λ_{em}: 308 nm) was used to better comprehend the Cu^{2+} sequestering abilities of any ligand[44]. Interestingly, the close vicinity of Cu^{2+} associated with Aβ_{42} causes fluorescence quenching of ^{10}Tyr at 308 nm, and this effect has been studied widely[45]. The fluorescence restoration of ^{10}Tyr at 308 nm is anticipated following the Cu^{2+} ion extraction by AOX from the Aβ_{42}−Cu^{2+} complex. The fluorescence intensity depicts the metal chelation capacity of AOX to eliminate Cu^{2+} from Aβ_{42} (Fig. 1A and B). In AD, amyloid fibrillar aggregates are formed when disordered Aβ_{42} peptide clump together and folds into an arranged β-sheet form. These fibrils can then aggregate into larger structures called plaques, which can lead to the death of neuronal cells in the brain. One of the most well-known methods for developing AD-specific therapeutic agents is to prevent the production of fibrillar aggregates. Thus, the study prohibition of metal-independent and metal-dependent amyloid fibrillar aggregation was studied by performing Thioflavin T (ThT) assay, Bradford assay, Dot blot, and circular dichroism (CD) measurements to investigate the impact of AOX on the tendency of Aβ_{42} to fibrillar aggregate. ThT is a fluorescent molecular probe that exhibits limited fluorescence with Aβ_{42} peptide and increased fluorescence intensity when bound with Aβ_{42} fibrillar aggregates (λ_{ex}: 450 nm and λ_{em}: 485 nm). The impact of AOX on the copper-independent and copper-dependent fibrillization of Aβ_{42} was therefore investigated using the ThT assay. In copper-independent fibrillar aggregation, Aβ_{42} peptide (10 μmol/L) was incubated alone (control) and also with various concentrations of AOX (0.5, 1, 2, 5, or 10 μmol/L) with constant agitation in the vortex for 72 h. After that freshly prepared ThT solution (50 μmol/L) was added, and the fluorescence intensity of the resultant mixture was measured. The result showed AOX inhibits 61.85% copper independent Aβ_{42} fibril formation at 0.5 μmol/L (17.9 ± 5.3), 1 μmol/L (33.5 ± 1.2), 2 μmol/L (41.3 ± 3.9), 5 μmol/L (50.8 ± 9.3) and 10 μmol/L (61.9 ± 5.1) concentration (Fig. 1C). In copper-dependent fibrillar aggregation, Aβ_{42} peptide (10 μmol/L) was co-incubated with Cu^{2+} solution (10 μmol/L) and also with various concentrations of AOX (0.5, 1, 2, 5, or 10 μmol/L) with constant hesitation in vortex for 72 h. The result showed the percentage activity of AOX inhibition at 0.5 μmol/L (10.8 ± 6.5), 1 μmol/L (25.8 ± 2.2), 2 μmol/L (33.3 ± 5.9), 5 μmol/L (40.3 ± 6.1) and 10 μmol/L (48.8 ± 2.7) concentration (Fig. 1D). So, this assay gives a clear understanding of the potential of AOX in the prohibition of metal ion-independent and metal ion-dependent amyloid fibrillar aggregation. Next, we performed a Bradford assay to determine the Aβ_{42} peptide content in the fibrilization process. In copper-independent fibrillar aggregation, Aβ_{42} peptide (10 μmol/L) was incubated alone (Aβ_{42} aggregates) and also with various concentrations of AOX (0.5, 1, 2, 5, or 10 μmol/L) with constant hesitation in vortex for 72 h. After that the resultant mixtures were centrifuged at 12,000 rpm to remove fibrillar aggregates and the filtrate containing Aβ_{42} peptides was incubated with Bradford reagent. Next, the absorbance intensity of the resultant solution was measured at 595 nm. Freshly prepared Aβ_{42} peptide was taken as a control. The results showed that the percentage activity for the copper-independent Aβ_{42} inhibition of AOX at 0.5 μmol/L (53.1 ± 9), 1 μmol/L (63.7 ± 2.4), 2 μmol/L (68 ± 2.5), 5 μmol/L (76.9 ± 4.7) and 10 μmol/L (88.6 ± 2.5) concentration but without AOX there was 41.04% Aβ_{42} peptide (Fig. 1E). In copper-dependent fibrillar aggregation, Aβ_{42} peptide (10 μmol/L) was co incubated with Cu^{2+} solution (10 μmol/L) to make copper induced fibrillar aggregates and also with various concentration of AOX (0.5, 1, 2, 5, or 10 μmol/L) with constant agitation in vortex for 72 h. The result showed that the percentage activity of AOX at 0.5 μmol/L (54.5 ± 4.9), 1 μmol/L (67.8 ± 1.7), 2 μmol/L (70.1 ± 3.2), 5 μmol/L (78.7 ± 5.9) and 10 μmol/L (91.3 ± 3.5) concentration without AOX there are 35.07% Aβ_{42} peptide (Fig. 1F).

The anti-aggregation property of AOX was verified using a dot blot assay. Three distinct antibodies were employed in this assay to identify the different amyloid species types. Anti-6E10 was used to detect all forms of Aβ species, anti-A11 was used to detect an oligomeric form of the amyloid species, and anti-OC was used to detect the amyloid fibril. For the control experiment, we incubated the Aβ peptide alone, whereas, for the inhibition experiment, various concentrations of AOX (0.5, 5, and or 10 μmol/L) were incubated with Aβ peptide (10 μmol/L) to see if this would prevent the production of oligomers and fibrils. Following Aβ peptide incubation, the solutions were spotted on three distinct sets of nitrocellulose membranes with two separate rows. The membrane spots' chemiluminescence intensity was evaluated and contrasted with that of the control experiment (Fig. 1G). The blotting test demonstrates that AOX was preventing the production of Aβ oligomers and fibrils. The small molecule AOX was limiting the formation of Aβ oligomers up to 76%−78% and Aβ fibrillation was inhibited up to 90%−94% at concentrations of 10 μmol/L, as shown by the intensity of spots in (Fig. 1H). Finally, we performed a CD experiment to measure the fibril inhibition by AOX by determining its changes in the secondary and tertiary structure. Here, the β-sheet structure is the measuring factor of fibrillar aggregate formation of the Aβ_{42} peptide. The negative ellipticity at 220 nm shows the β-sheet structure of Aβ_{42} fibrillar aggregates. In the presence of AOX, the negative ellipticity decreases and at 10 μmol/L concentration of AOX, the β-sheet structure is much less amount (Fig. 1I). As the molecule inhibits Aβ aggregation, we were interested in how the compound interacts with Aβ_{42} fibril and monomer. We have performed the docking study of the compound with fibril and monomer. The result shows that AOX is binding to the carbonyl oxygen of Isoleucine 31 by the hydrogen of the OH group through hydrogen bonding with a binding energy of −6.2 kcal/mol. About the fibril, the compound interacts with His13, His13, and Glu 11 through

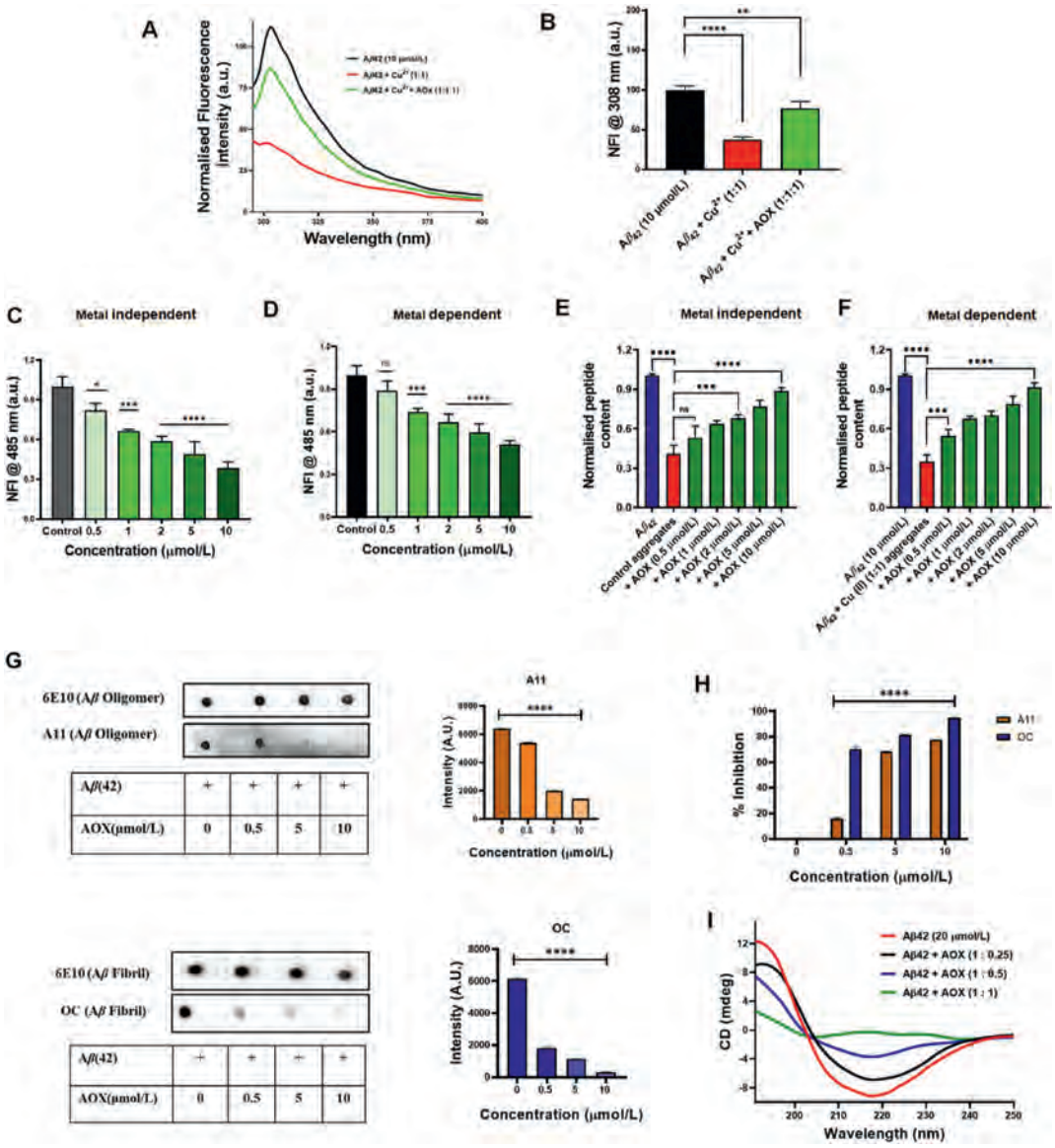

Figure 1 Determination of Aβ_{42} inhibition activity of AOX. (A) Fluorescence spectra of 10Tyr of only Aβ_{42} (10 μmol/L) and Cu^{2+}−Aβ_{42} (1:1) with and without AOX (10 μmol/L) in PBS. (B) Bar diagram of Fluorescence spectra of 10Tyr of only Aβ_{42} (10 μmol/L) and Cu^{2+}−Aβ_{42} (1:1) with and without AOX (10 μmol/L) in PBS. (C, D) ThT assay for amyloid fibril inhibition showing bar diagram of copper independent and dependent fibril prevention of Aβ_{42} peptide (10 μmol/L) by AOX compound with various concentrations (0.5, 1, 2, 5, and 10 μmol/L). (E, F) Bar diagram of Aβ_{42} peptide amount determined by AOX compounds with copper independent and copper-dependent fibril prevention using Bradford assay. (G, I) Dot blot assay for amyloid fibril and amyloid oligomer inhibition in the presence of AOX in different concentrations. (H) Bar diagram of dot blot assay for amyloid fibril and amyloid oligomer percentage inhibition. Error bar related to standard deviation of the value (ns = non-significant, $*P < 0.05$, $**P < 0.01$, $***P < 0.001$, $****P < 0.0001$).

H-bonding with binding energy −7.6 kcal/mol (Supporting Information Fig. S14). Therefore, the negative binding energy confirms the interaction of AOX with monomer and fibril which inhibit the toxic amyloid aggregates. From all of the above experiments, it was clear that AOX reduces the metal-independent and metal-dependent amyloid fibrillar aggregation.

2.3. *In vitro antioxidant properties of AOX*

To assess the antioxidant activity of our novel small molecule AOX and to confirm its potential for further therapeutic actions in the reduction of oxidative damage and its associated detrimental effects, various biophysical *in vitro* assays like, DPPH (2,2-diphenyl-1-picrylhydrazyl), ABTS (2,2′-azino-bis (3-ethylbenzothiazoline-6-sulphonic acid), Nitric oxide scavenging, protein oxidation and CCA (Coumarin-3-carboxylic acid) assays were conducted.

DPPH assay is widely used for preliminary evaluation of the antioxidant activity of small molecules. It is a stable free radical at room temperature and becomes a stable diamagnetic molecule on accepting an electron or hydrogen radical[46]. Therefore, this assay was performed to check the ability of AOX to scavenge the stable free radical. In (Fig. 2A), its mechanism of action with DPPH shows that the purple colour DPPH radical is reduced to pale

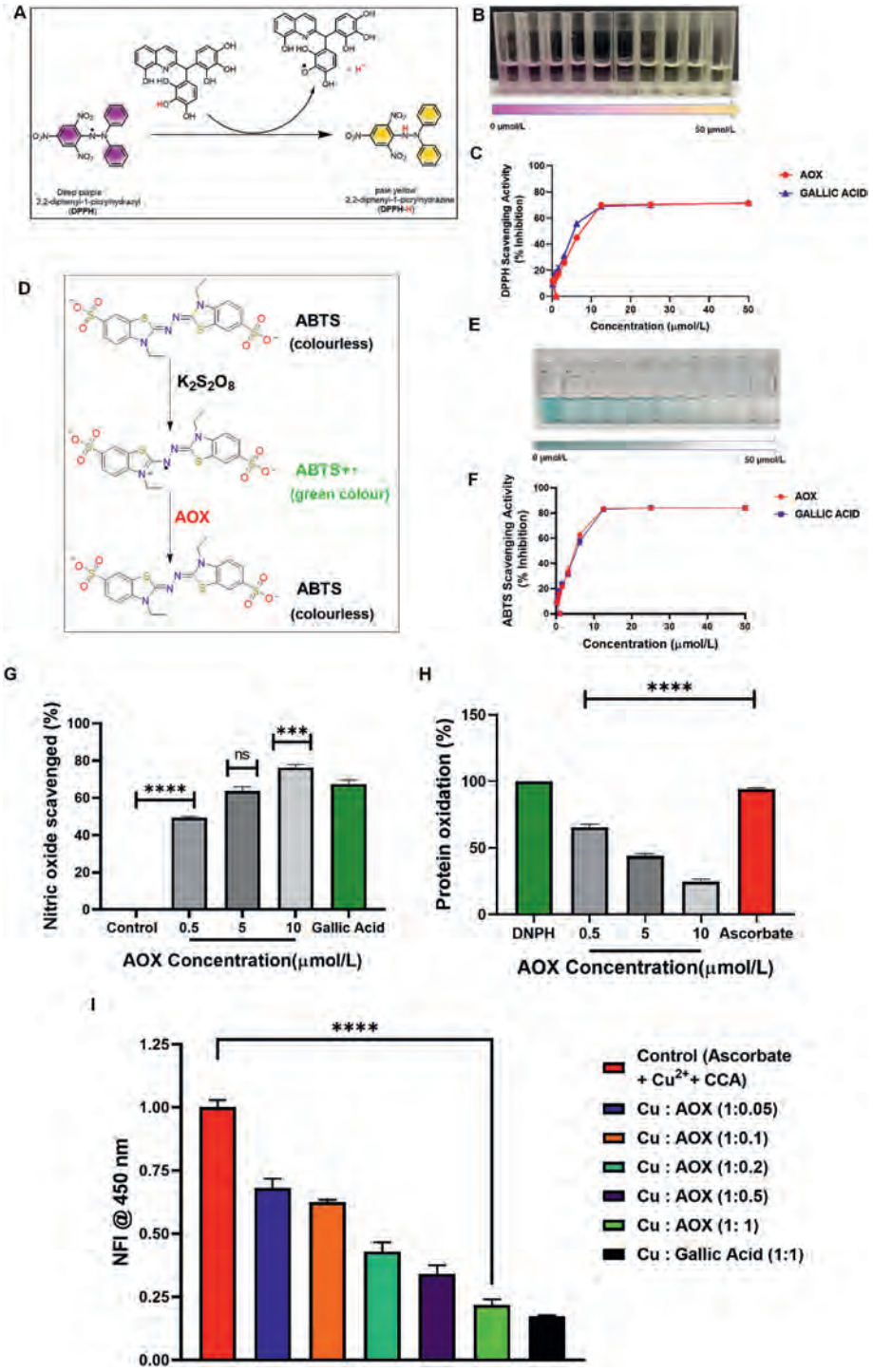

Figure 2 Determination of *in vitro* Antioxidant activity of AOX. (A) Schematic representation of the chemical structure of DPPH and its reduction by AOX. (B) DPPH Absorption spectra (400−800 nm) medium for various concentrations of AOX (0−50 µmol/L) and DPPH. (C) DPPH radical scavenging effects of various equal concentrations of AOX and gallic acid. (D) Schematic representation of the chemical structure of ABTS and its reduction by AOX. (E) Image of reduction of ABTS, when reacted with increasing concentration of AOX (0−50 µmol/L). (F) ABTS radical scavenging activity of various equal concentrations of AOX and gallic acid (0−50 µmol/L). (G) Radical Scavenging activity of AOX, analyzed through nitric oxide. (H) Percentage of BSA oxidation was assessed and quantified by measuring DNPH absorption at 450 nm. (I) Bar diagram of normalized fluorescence intensity of 7-OH-CCA after 70 min. Error bar related to standard deviation of the value (ns = non-significant, $*P < 0.05$, $**P < 0.01$, $***P < 0.001$, $****P < 0.0001$).

yellow colour. It is evident from (Fig. 2B), that the DPPH radical concentration in the reaction medium is reduced in a gradient manner with increasing concentration of AOX when assessed spectrophotometrically with the maximum absorption at 517 nm (Supporting Information Fig. S15). The result of the assay showed that the *in vitro* free radical potential of AOX exhibited maximum free radical scavenging activity with EC_{50} (effective concentration that results in a 50% reduction in the initial DPPH concentration) value of a comparable known standard, Gallic acid. Therefore, to quantify the result, EC_{50} was calculated by plotting a dose−response linear fit graph on OriginPro 8.5 (Supporting Information Fig. S16). The EC_{50} value calculated for gallic acid was 8.63357 μmol/L whereas for AOX it was 4.86324 μmol/L. The percentage inhibition was calculated for both AOX and gallic acid (Fig. 2C). It has been seen that certain bioactive compounds are not soluble in the reaction medium and may not express true radical scavenging activities. Therefore, to rule out the antioxidant activity in the methanolic medium using DPPH we performed an ABTS radical scavenging assay which is carried out in an aqueous medium. Schematic representation of the ABTS radical scavenging method in the presence of various concentrations of AOX (0, 0.19, 0.39, 0.078, 0.15625, 3.125, 6.25, 12.5, 25, and 50 μmol/L) shows the purple colour solution change to colourless (Fig. 2D and E). Absorbance spectra of $ABTS^{\cdot+}$ solution with the addition of AOX and gallic acid were recorded from 400 to 900 nm and the characteristic absorption peak was recorded at 734 nm (Supporting Information Fig. S17). The percentage inhibition was calculated by comparing the result with standard (gallic acid) at various concentrations as shown in (Fig. 2F). The EC_{50} value calculated for gallic acid was 5.333 μmol/L whereas for AOX it was 4.8611 μmol/L.

Nitric oxide (NO) molecule serves as a signalling molecule in various physiological processes. Where NO is not considered as a free radical rather it interacts with other molecules to form harmful reactive nitrogen species, such as peroxynitrite ($ONOO^-$), which contributes to oxidative stress. Therefore, the scavenging of NO by antioxidants is important for reducing nitrosative stress, limiting the formation of harmful reactive nitrogen species (RNS), and protecting the cells and tissues from oxidative damage[47]. We evaluated the nitric oxide scavenging ability of various concentrations of AOX and gallic acid standard (10 μmol/L) using Griess assay. In this assay, the quantity of nitrite that forms when oxygen and NO are produced from sodium nitroprusside is reduced. At 548 nm, the absorbance was measured, and the antioxidant activity percentage was calculated. Interestingly, AOX showed a 76.3% reduction in NO generation whereas Gallic acid showed a 67.47% reduction with similar concentration (Fig. 2G). Next, we assessed the protein oxidation percentage which is characterized by the formation of protein carbonyls as a result of the detrimental effect of ROS. The measurement of carbonyls provides a quantitative approximation of the extent of oxidation and is done by using DNPH (2,4-dinitrophenylhydrazine). DNPH reacts with carbonyl groups in oxidized proteins to form hydrazones, which are spectrophotometrically detected by monitoring the absorbance intensity at 450 nm[48]. To evaluate the protective effect of AOX, the protein oxidation was carried out by hydroxyl radical generation using a metal catalysed system by a Fenton-type reaction. Where BSA was used to mimic the cellular protein, and Cu^{2+} (0.1 mmol/L) and H_2O_2 (2.5 mmol/L) were used as redox systems for the generation of ROS. To the solution mixture of BSA (1 mg/mL) with AOX and Gallic acid standard prepared in PBS buffer was added with Cu^{2+} and H_2O_2 and incubated in the dark for 24 h. After incubation DNPH solution was added and incubated for 10 min the absorption was recorded at 450 nm and the protein oxidation percentage was calculated. The DNPH control (BSA and $Cu^{2+} + H_2O_2$) sample showed maximum absorption at 450 nm and showed no protein inhibition. Whereas, a solution with AOX (0.5, 5 and 10 μmol/L) reduced the protein oxidation inhibition in a concentration-dependent manner (34.5%, 56% and 75% respectively). Where these results suggest that AOX effectively scavenges ROS as compared to ascorbate which inhibited protein oxidation by only 6% (Fig. 2H). Finally, the copper-induced ROS inhibition of AOX was studied by CCA (Coumarin-3-carboxylic acid) assay. In the presence of Ascorbate, Cu^{2+} ion produces OH radical which further reacts with nonfluorescent CCA to form fluorescent 7-OH-CCA (λ_{ex}: 385 nm and λ_{em}: 450 nm). In the presence of AOX, the quantity of OH radical was reduced and finally, the amount of fluorescent 7-OH-CCA was also decreased. The experimental results indicated that the fluorescence intensity of 7-OH-CCA increases with time and saturated up to 70 min with the time of the control experiment (without AOX), but in the presence of an increasing concentration of AOX the fluorescence intensity gradually decreases (Supporting Information Fig. S18). The graph plotted in Fig. 2I showed AOX inhibiting 78.19% of OH radical formation at 10 μmol/L concentration (0.5 μmol/L: 31.96%, 1 μmol/L: 37.52%, 2 μmol/L: 57.09% and 5 μmol/L: 65.83%).

2.4. Effect of H_2O_2 mediated oxidant treatment on viability and intracellular oxidative stress on AOX pre-treated differentiated PC12 (dPC12) cells

Neuroprotective and antioxidative activity of AOX was studied in the PC12 cell derived neuronal model[49]. Hydrogen peroxide is widely used as an oxidant to generate oxidative stress models in various cell lines including PC12 cells. A series of dose−response experiments have been performed for an appropriate concentration of H_2O_2 so that a stable and optimized concentration is determined. As shown in Fig. 3A, the concentration of 200 μmol/L H_2O_2 for 2 h resulted in a decline of cell viability of dPC12 cells by approximately 50%. Thus, this concentration and time of treatment were employed as the oxidant model condition. Prior to initiating any cellular assays to evaluate the antioxidant potential of the newly synthesized small molecule AOX, a comprehensive assessment of media stability was imperative. Using RP-HPLC analysis, we found that AOX remained 93% stable for up to 24 h in the cell culture media. This meticulous stability testing ensured that the compound maintained its chemical integrity within the media environment, laying a solid groundwork for reliable and accurate cellular assays (Supporting Information Fig. S19). Reactive oxygen species (ROS) exhibit a dual role in cellular physiology, acting as both mediators of oxidative stress and essential signaling molecules[50]. While ROS are commonly associated with cellular damage and disease pathology, it is increasingly recognized that they also play important roles in cellular signaling pathways involved in cell proliferation, differentiation, and immune response. ROS serve as secondary messengers, modulating the activity of transcription factors and signaling pathways such as NF-κB, MAPKs, and Nrf2. However, complete elimination of ROS can disrupt these signaling pathways and lead to paradoxically detrimental effects on cellular function, including impaired immune responses, dysregulated cell proliferation, and increased susceptibility to oxidative stress-induced damage. To demonstrate that beneficial ROS are not eliminated,

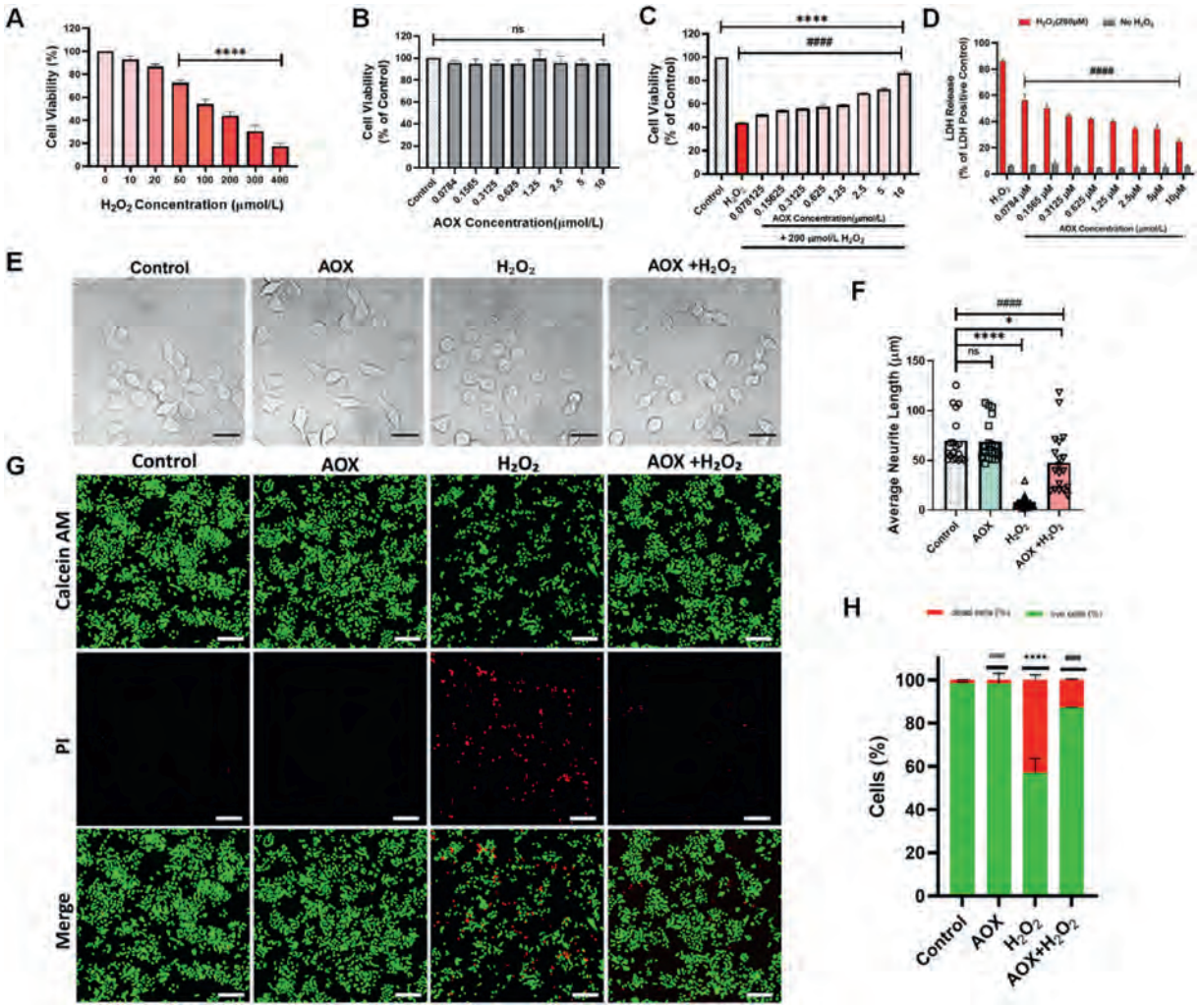

Figure 3 Effects of AOX on H2O2-induced oxidative stress in dPC12 cells. (A) dPC12 cells were treated with 0, 10, 20, 50, 100, 200, 300, or 400 μmol/L H_2O_2 for 2 h, and then cell viability was determined using MTT assay (B) Cells were treated with various concentrations of AOX for 24 h, and then cell viability was determined by MTT assay. (C) Cells were pre-treated with various concentrations of AOX for 24 h, then 200 μmol/L of H_2O_2 was added. After incubation for 2 h, an MTT assay was used to check the cell viability (%). (D) LDH release in the culture medium was measured using the LDH Colorimetric Assay Kit. (E) Morphology of dPC12 cell line. Control- Untreated, treated with 10 μmol/L AOX, treated with H_2O_2 (200 μmol/L) for 2 h, treated with AOX (10 μmol/L) for 24 h followed by H_2O_2 (200 μmol/L) for 2 h. (F) Average neurite length calculated for treated cells. (G) Calcein AM and propidium iodide staining to assess cell viability by fluorescence imaging. Scale bar corresponds to 50 μm (H), the percentage of dead and live cells was calculated by mean normalized fluorescence intensity. Calcein AM represents live cells, whereas PI represents dead cells. The results are represented as the mean ± SEM. $n = 3$ per group and $n = 19$ per group for (F). $^{****}P < 0.0001$ *versus* the control group, $^{\#\#\#\#}P < 0.0001$ *versus* the H_2O_2 group. Data were analyzed using a one-way analysis of variance.

we conducted MTT and LDH assays. The MTT assay measures cell viability by assessing the reduction of a yellow tetrazolium salt to formazan crystals by metabolically active cells, while the LDH assay measures cytotoxicity by quantifying the release of lactate dehydrogenase enzyme from damaged cells. The results of these assays corroborate our findings, indicating that while modulation of ROS levels occurred, cellular viability and integrity were maintained. These experiments provide further evidence supporting the nuanced role of ROS in cellular physiology and highlight the importance of maintaining ROS homeostasis for cellular health. Understanding the complex interplay between ROS signaling pathways is crucial for developing novel therapeutic interventions for neurodegenerative disorders and other oxidative stress-related diseases, aiming to restore redox balance and protect against cellular damage. The cytotoxic effect of various concentrations of AOX was determined using an MTT assay. Where, AOX shows non-significant toxicity at lower (0.078 μmol/L) as well as at higher concentration (200 μmol/L) (Fig. 3B and Supporting Information Fig. S20). Next, the neuroprotective effect was evaluated by 24 h pre-treatment of the dPC12 cells with various concentrations of AOX followed by 2 h oxidant treatment. Thus, calculating the percentage recovery of the cells from oxidative damage, AOX showed a dose-dependent recovery from the oxidative damage with 10 μmol/L showing approximately 75% recovery (Fig. 3C). Sequentially performing the LDH (lactate dehydrogenase) assay following the MTT assay provides a comprehensive approach to assessing the cell viability and cytotoxicity in terms of cell membrane integrity unlike the

MTT assay which measures the metabolic activity. Therefore, performing these assays in combination provided a more holistic approach to strengthen the reliability of our findings observed due to biological effects, and thus the results could be cross-validated. LDH enzyme leakage content in the culture medium in the presence of oxidant was elevated as a mark of cellular injury or death. On the other hand, AOX pre-treated cells with/without oxidant mitigated oxidative stress and prevented cellular damage by neutralizing the ROS generated due to oxidant. Therefore, a quantitative measure of the cellular damage was evaluated in Fig. 3D and Supporting Information Fig. S21 to aid in evaluating the effectiveness of AOX in protecting against oxidative-stress-related injuries. To confirm the cell viability data a subsequent morphological experiment was conducted with the same experimental conditions. In Fig. 3E the morphology of the dPC12 cells is studied for a better understanding of cellular responses to oxidative stress and the potential neuroprotective effect of AOX, which showed healthy morphology of the cells with neurite outgrowth in the control and AOX-treated group depicting the non-toxic effect of AOX to the dPC12 cells, whereas it can be seen that when cells were treated with H_2O_2 the cells no longer show a distended morphology of a neuron rather they become round with fragmented nucleus, compromised membrane and retracted neurites. In the same oxidant condition of cells pre-treated with AOX does not show the apoptotic effect of the cells rather healthy morphology with extended neurites can be seen. The calculation of neurite length in the presence of oxidant (H_2O_2) and antioxidant (AOX) serves as a quantitative measure to elucidate the impact of oxidative stress on the morphology of the neurons and the neuroprotective potential of the novel antioxidant small molecule. Therefore, the calculations supported the hypothesis that AOX mitigates the adverse effects of oxidative stress on neuronal morphology (Fig. 3F), and a decrease in neurite length was observed in the presence of an oxidant, indicating a potential neurotoxic effect. Calcein AM, a cell-permeate dye is converted to its fluorescent form by intracellular esterases in live cells emitting green fluorescence. Whereas, propidium iodide (PI), a cell-impermeant dye penetrates only non-viable cells with compromised cell membranes emitting red fluorescence after binding to the nucleic acids. In Fig. 3G, fluorescence images provide a quantitative measure of cellular viability by differential uptake of these fluorescent dyes by live and dead cells. When AOX pre-treated cells were introduced with oxidant, a notable outcome in terms of increased live cells was seen as indicated with higher Calcein AM fluorescence and a decrease in dead cells reflected by lower PI fluorescence. A quantitative analysis was performed in Fig. 3H to calculate the ratio of live and dead cells, providing a more nuanced understanding of AOX efficacy. The one-way ANOVA statistical method was applied to determine the significance of the observed differences between the group's data. These results further offered an insight into the mechanism underlying antioxidant-mediated protection against oxidative stress which was studied further in detail.

2.5. Probing ROS accumulation inhibition in the presence of AOX and H_2O_2-induced oxidative stress

As shown previously AOX protects dPC12 cells from H_2O_2-induced oxidative damage. Therefore, due to the presence of various hydroxyl groups in our novel antioxidant small molecule (AOX) it is evident that it will also have an efficient free radical neutralizing ability. The presence of excess ROS induces cell apoptosis and causes DNA damage. So, to provide a comprehensive evaluation and quantitative measure of ROS levels within cells a targeted analysis was performed to understand the oxidative stress environment, and the potential of AOX's effectiveness across various cellular compartments was studied for an overall impact on cellular redox balance. DCFDA (2′,7′-dichlorodihydrofluorescein diacetate), CellROX, and MitoSOX assays were employed to identify the specific sites of ROS production and its mitigation in the cytoplasm, overall cellular environment and mitochondria, respectively. DCFDA, a cell-permeate fluorophore diffuses into the cells and is deacetylated by cellular esterases to a non-fluorescent 2′,7′-dichlorodihydrofluorescin (DCFH), and in the presence of ROS, it is oxidized to a highly fluorescent species dichlorodihydrofluorescin (DCF). The fluorescence intensity of the cell was measured using a microplate reader with excitation/emission at 485 nm/535 nm. The results are represented as a percentage of fluorescence intensity relative to control which measured a broad spectrum of ROS in cytoplasm. As shown in Fig. 4A, H_2O_2 promotes ROS overproduction in dPC12 cells as compared to control. However, 24 h pre-incubation with varied concentrations of AOX followed by H_2O_2 treatment notably reduced ROS by inhibiting the intracellular ROS with no significance compared to control. Furthermore, fluorescence imaging to examine the fluorescence intensity of ROS levels in H_2O_2 induced damage to dPC12 cells with pre-treated AOX (10 μmol/L) was quantified by fluorescence imaging and flow cytometry (Fig. 4B and C, Supporting Information Fig. S22). The fluorescence intensity obtained was directly proportional to the amount of ROS present. More specific detection of intracellular ROS levels in live cells was done with CellROX deep red stain, a cell-permeable fluorogenic probe. In Fig. 4D, an increase in cellROX fluorescence was seen in H_2O_2 treated dPC12 indicating elevated levels of ROS as compared to AOX pre-treated and H_2O_2 group where it attenuated the increase in CellROX fluorescence intensity. Mean fluorescence intensity was calculated as a quantitative measure of the amount of fluorescence signal present in the given region of interest (Fig. 4E). Further, we assessed the mitochondrial impairment due to oxidative stress inducers and the impact of AOX on this condition. Mitochondrial superoxide production was detected with MitoSOX red fluorogenic dye. The intensity of the fluorescence signal directly correlated with the amount of superoxide present in the mitochondria. Relative quantification of its fluorescence intensity was also measured to calculate the amount of mitochondrial superoxide generated under different experimental conditions as shown in Fig. 4F and G. A higher intensity was observed in the oxidant group when compared to the untreated control group. Conversely, AOX leads to a reduction in the intensity showing its effectiveness in the protection of mitochondrial integrity.

2.6. Alleviation of H_2O_2-induced apoptosis by AOX

Based on the efficient ROS neutralizing ability of AOX *in vitro*, we then further explored the mechanism of the antioxidant enzymes and their interplay with AOX in understanding cellular defence mechanisms against oxidative stress. As illustrated in Fig. 5A by a schematic representation of the mechanism of action of the antioxidant enzymes, oxidative stress and lipid peroxidation markers involving superoxide dismutase (SOD), catalase (CAT), glutathione peroxidase (GPx), reduced glutathione (GSH) and malondialdehyde (MDA) forming a well-orchestrated network crucial for cellular defence. An elevation in oxidative stress leads to increased production of ROS which leads to enhanced lipid

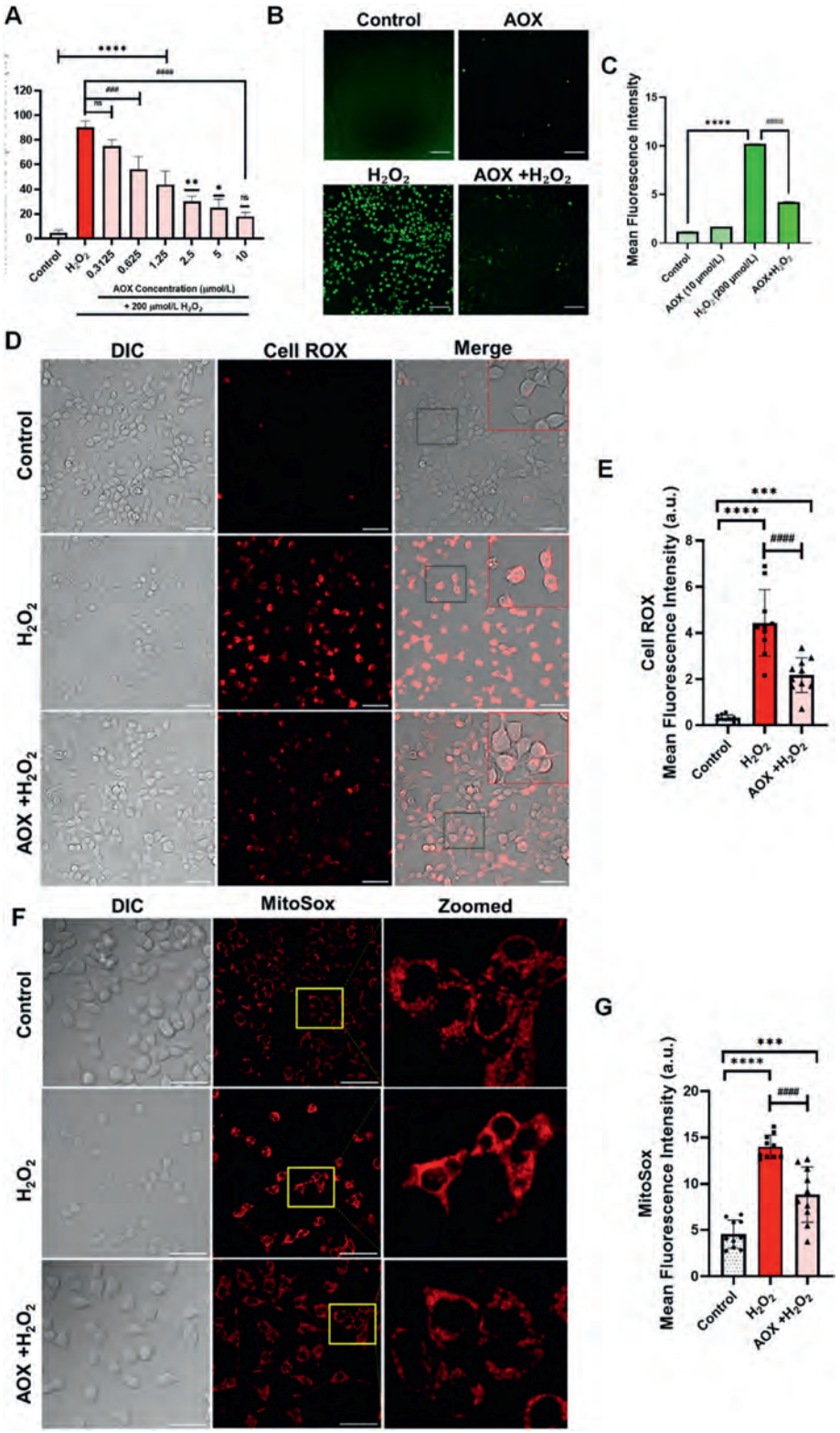

Figure 4 Effects of AOX in mitigating the total ROS in H_2O_2 induced oxidative stress in dPC12 cells. (A) Intracellular ROS production percentage analysis by DCFH-DA staining using a microplate reader. (B) Fluorescent microscopy images of DCFH-DA. (C) Mean fluorescence intensity bar graph corresponding to the microscopy images. (D) CellROX Deep Red staining assay shows an increase in intracellular levels of ROS (red fluorescence) in H_2O_2-treated PC12 cells whereas AOX reduces its level significantly. (E) Relative quantification of CellROX red fluorescence. (F), (G) Mitochondrial superoxide production was detected with MitoSOX red staining and relative quantification was done by ImageJ software. The results are represented as the mean ± SEM. $n = 3$ per group for (A) and $n = 10$ for (E, G). $^{**}P < 0.01$, $^{****}P < 0.0001$ *versus* the control group, $^{\#\#}P < 0.01$ $^{\#\#\#\#}P < 0.0001$ *versus* the H_2O_2 group. Data were analyzed using a one-way analysis of variance. Scale bar corresponds to 50 µm.

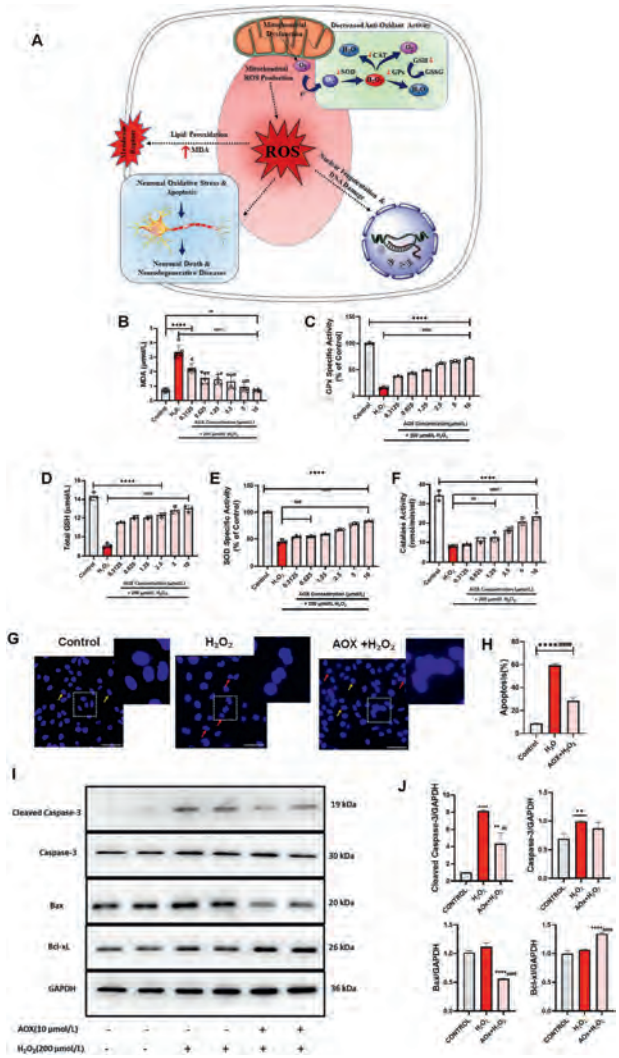

Figure 5 Determining the effects of AOX in enhancing the antioxidant mechanism and alleviating the cellular apoptosis in H_2O_2 induced oxidative stress in dPC12 cells. (A) Schematic illustration of the mechanism of action of antioxidant enzymes in oxidative stress condition. Effect of AOX on the activities of (B) MDA (C) GPx, (D) GSH, (E) SOD, and (F) catalase in PC12 cells. PC12 cells were pretreated with AOX for 24 h and then exposed to H_2O_2 (200 μmol/L) for 2 h. The activities were measured using kit assays according to the manufacturer's instructions. (G) Morphological assessment of apoptosis observed by Hoechst 33258 staining using a fluorescence microscope. Yellow arrows indicated normal nuclei and red arrows indicated apoptotic nuclei. (H) Bar graph representation of the percentage of apoptotic cells calculated. (I) Expression of anti-apoptotic and pro-apoptotic protein was evaluated by Western blot. (J) Quantitative analysis of cleaved-caspase-3, caspase-3, Bax, and Bcl-xL, protein levels in PC12 cells, GAPDH serves as the housekeeping protein in Western blot assay. The results are represented as the mean ± SEM ($n = 5$ or $n = 3$) per group. $^{**}P < 0.01$, $^{****}P < 0.0001$ *versus* the control group, $^{\#\#}P < 0.01$ $^{\#\#\#\#}P < 0.0001$ *versus* the H_2O_2-treatment group. Data were analyzed using a one-way analysis of variance. Scale bar corresponds to 50 μm.

peroxidation and subsequently higher levels of MDA. Whereas antioxidant enzymes like SOD initiates the cascade by converting superoxide radicals into hydrogen peroxide and oxygen, CAT further neutralizes hydrogen peroxide into water and oxygen, and GPx utilizes GSH as a cofactor to efficiently detoxify hydrogen peroxide and lipid peroxides, forming oxidized glutathione (GSSG). When AOX was introduced in this intricate network of antioxidant enzymes it added a dynamic element in the cellular defence against oxidative stress to counteract this oxidative damage by neutralizing ROS and preventing lipid peroxidation. As shown in Fig. 5B, the production of MDA level was found to be reduced in the dose-dependent treatment with AOX, which was much lower than that in the only H_2O_2 treated group. One of the most significant byproducts of membrane lipid peroxidation, MDA level influences the function of respiratory chain complexes as well as essential mitochondrial enzymes. Both glutathione peroxidase (GPx) and superoxide dismutase (SOD) are significant antioxidative enzymes in the human body that effectively neutralise reactive oxygen species (ROS) to repair cells and reduce ROS-induced damage. In this study, we then further examined the changes in the level of SOD, CAT, GPx, and GSH activity from the standard curve equations plotted for each enzyme in Supporting Information Fig. S23. As shown in Fig. 5C and D, in the presence of an oxidant GPx activity rises as it works to detoxify hydrogen peroxide and lipid peroxidation by utilizing GSH as a substrate whereas in the presence of AOX, its activity is stabilized and increased as AOX effectively neutralizes oxidants and preserve GSH levels by preventing its excessive consumption. SOD level is elevated with increasing dose of AOX in the presence of oxidant and was much higher than that in the oxidant group alone (Fig. 5E). This outcome was due to the increased conversion of superoxide radicals to hydrogen peroxide and oxygen in the presence of AOX which enhanced its activity by accelerating the dismutation of superoxide radicals. Enhanced catalase activity in the presence of AOX and oxidants positively influenced its levels by directly interacting with the enzymes for efficient detoxification of hydrogen peroxide when compared to the oxidant group to impact the overall cellular redox balance (Fig. 5F). DNA damage and nuclear fragmentation are closely associated with oxidative stress. Therefore, the percentage of apoptotic differentiated PC12 cell population was determined by fluorescence microscopy after Hoechst 33258 staining. In Fig. 5G and H, the control group cells showed normal morphology with no irregularities in the shape of nuclei or apoptotic bodies. In the H_2O_2 group, the nuclei showed distinctive changes in nuclear morphology with irregularities, apoptotic features, cellular shrinkage, and heterogeneity in nuclear size due to the impact of the oxidant-induced stress on the cellular integrity. In contrary to the oxidant group, the AOX pretreatment group displayed a morphology closer to untreated cells, indicating a protective effect. We further aimed to determine whether AOX could suppress apoptosis-mediated neuronal death. Caspase 3 and cleaved caspase-3 are widely used to evaluate the apoptosis level. Western blot analysis displayed that AOX pretreatment suppresses the effect of oxidants and imparts antioxidative effects. The expressions of the anti-apoptotic protein Bcl-xL were upregulated and that of pro-apoptotic protein Bax was downregulated after treatment with AOX (Fig. 5I and J, Supporting Information Fig. S24).

2.7. Assessing dynamic interplay of AOX in H_2O_2-induced oxidative stress on mitochondrial morphology and membrane potential

Mitochondria play a central role in cellular energy production and overall cell function. Assessing the impact of oxidative stress in the presence of a novel potent antioxidant influences mitochondrial morphology to provide an insight into the impact of cellular health. A hallmark of cells going through apoptosis is mitochondrial malfunction and results in altered mitochondrial morphology. It serves as an early biomarker to screen for an effective antioxidant showing neuroprotective therapies by reversing the altered mitochondrial morphology caused by the neurodegenerative processes. The DNA damage, cellular architecture, and altered mitochondrial morphology were analyzed by staining dPC12 cells after indicated treatments with Hoechst 33258/Phalloidin/Mitotracker CMX-ROS and were viewed under a fluorescent microscope (Supporting Information Fig. S25). To specifically visualize the mitochondria, MitoTracker CMX-ROS stain images were deconvulated for image acquisition. The mitoTracker red signals were further made binary and thresholded for analyzing the particle followed by skeletonizing it which quantified the mitochondrial morphometrics using four parameters: number of mitochondria, size, interconnectivity, and elongation (as mentioned in the methods section). In untreated dPC12 cells, most of the mitochondria were interconnected with a greater average size which was measured by the interconnectivity score, which signified that the mitochondria have more physical connection. Whereas, in the oxidant group the interconnectivity score was significantly lower as compared to the control group, signifying mitochondrial fragmentation and the shape of mitochondria exemplary of the puncta, rod, network, and large and round subtypes accounted to the mean elongation data where higher values indicated more abstract shape and a value of 1 was considered more circular as in the case of oxidant group where cells were rounded to due oxidative stress. Contrary to this, pre-treatment with AOX showed the morphometric data of mitochondria to be very close to that of the control showing the protective effect (Fig. 6A−F). Next, mitochondrial membrane potential (MMP, $\Delta\psi_m$) was detected by JC-1 fluorescent dye, which is sensitive to MMP. JC-1 monomer shows green fluorescent with the excitation and emission of 485 and 535 nm and tends to accumulate in the mitochondrial matrix of unhealthy cells. Whereas, JC-1 aggregates show red fluorescence with the excitation and emission of 560 and 595 nm under the condition of high MMP of healthy cells. In apoptotic cells, JC-1 remains in monomeric form due to mitochondrial dysfunction under the condition of low mitochondrial potential. Thus, the mitochondrial depolarization can be measured by the extent of red to green (aggregate/monomer) fluorescence shift. Flow cytometry analysis as well as the fluorescent images in Fig. 6G and I, respectively, of mitochondria showed red fluorescence in control untreated differentiated PC12 cells showing active mitochondria, but H_2O_2 treated cells showed decreased MMP by the enhancement of the green fluorescence and reduced red fluorescence. Whereas, AOX treatment in the presence of H_2O_2 alleviated the red fluorescence significantly. A positive control of FCCP was employed to study the lost mitochondrial membrane integrity by the induction of depolarization of MMP. Fluorescence intensity was quantified in each group using ImageJ software (Fig. 6H and J).

2.8. AOX attenuates oxidative stress by activating the Nrf2/ARE signaling pathway

Nrf2 (nuclear factor erythroid 2-related factor 2) is a transcription factor that regulates the expression of antioxidant genes, and ARE (antioxidant response element) is a DNA sequence that responds to Nrf2, promoting the transcription of protective antioxidant enzymes. Therefore, we further explored whether pre-treatment with AOX could promote the activation of the Nrf2/ARE signalling pathway, known for its critical cellular defence mechanism against oxidative damage, and block the activation of oxidative stress and apoptosis-mediated cell death in oxidant-treated dPC12 cells. The schematic representation of Nrf2/ARE pathway activation provides a visual overview of the molecular events involved and the influence of AOX in the cellular response to oxidative stress by activating Nrf2 nuclear translocation leading to the upregulation of phase-II antioxidant enzymes (NQO1, HO-1, GCLC, and GCLM) for promoting cellular resilience and redox homeostasis (Fig. 7A). As shown by immunofluorescence staining with anti-Nrf2, AOX pre-treatment for 24 h followed by oxidant treatment of 2 h increased the fluorescence intensity of Nrf2 and promoted the translocation of Nrf2 to the nucleus from the cytoplasm (Fig. 7B). Therefore, by conducting Western blot analysis for both cytoplasmic and nuclear protein fractions we gained quantitative data on Nrf2 expression. In the absence of oxidant or AOX, Nrf2 was sequestered in the cytoplasm by KEAP1. Therefore, we observed a higher intensity of band in the cytoplasmic fraction for the control group. Whereas, a decrease in the cytoplasmic Nrf2 signal was seen in the AOX + oxidant group indicating enhanced translocation into the nucleus as compared to that of only the oxidant group (Fig. 7C). β-Actin was used as a loading control for normalizing the data and plotted in Fig. 7D and Supporting Information Fig. S26. In Fig. 7E, activation of Nrf2 was seen in the AOX + oxidant group by successful translocation of Nrf2 into the nucleus which was noticed with the increase in the intensity of the Nrf2 band in the nuclear fraction compared to the condition of only the oxidant group. Higher Nrf2 band intensity in the nuclear fraction indicated a higher concentration of activated Nrf2 in the nucleus suggesting a more robust activation of the Nrf2/ARE pathway. Lamin A/C was used as loading control for a nuclear fraction for normalizing the data and plotted in Fig. 7F and S26. This observation of better Nrf2 translocation in the presence of AOX was intriguing and motivated us to study the potential modulation of the Nrf2/ARE pathway. Western blot analysis shows the protein expression pattern of Nrf2, Keap-1, NQO1, HO-1, and catalase in the control and experimental groups (Fig. 7G). The band intensity was normalized with the GAPDH housekeeping gene and the levels of Nrf2, NQO1, HO-1, and catalase protein expression significantly increased in AOX pre-treated dPC12 cells in addition to oxidant treatment when compared to only oxidant and untreated control group with a significant decrease in Keap-1 protein (Fig. 7H and Supporting Information Fig. S27). Fig. 7I depicts the effect of AOX on the mRNA expression of Nrf2, NQO1, HO-1, GCLC, and GCLM in dPC12 cells control and experimental groups. The mRNA expression of Nrf2, NQO1, HO-1, and its downstream proteins such as GCLC and GCLM significantly decreased in H_2O_2-induced oxidative stress in dPC12 cells. However, the altered mRNA expressions were significantly prevented by the pre-treatment with AOX on H_2O_2-induced oxidative stress.

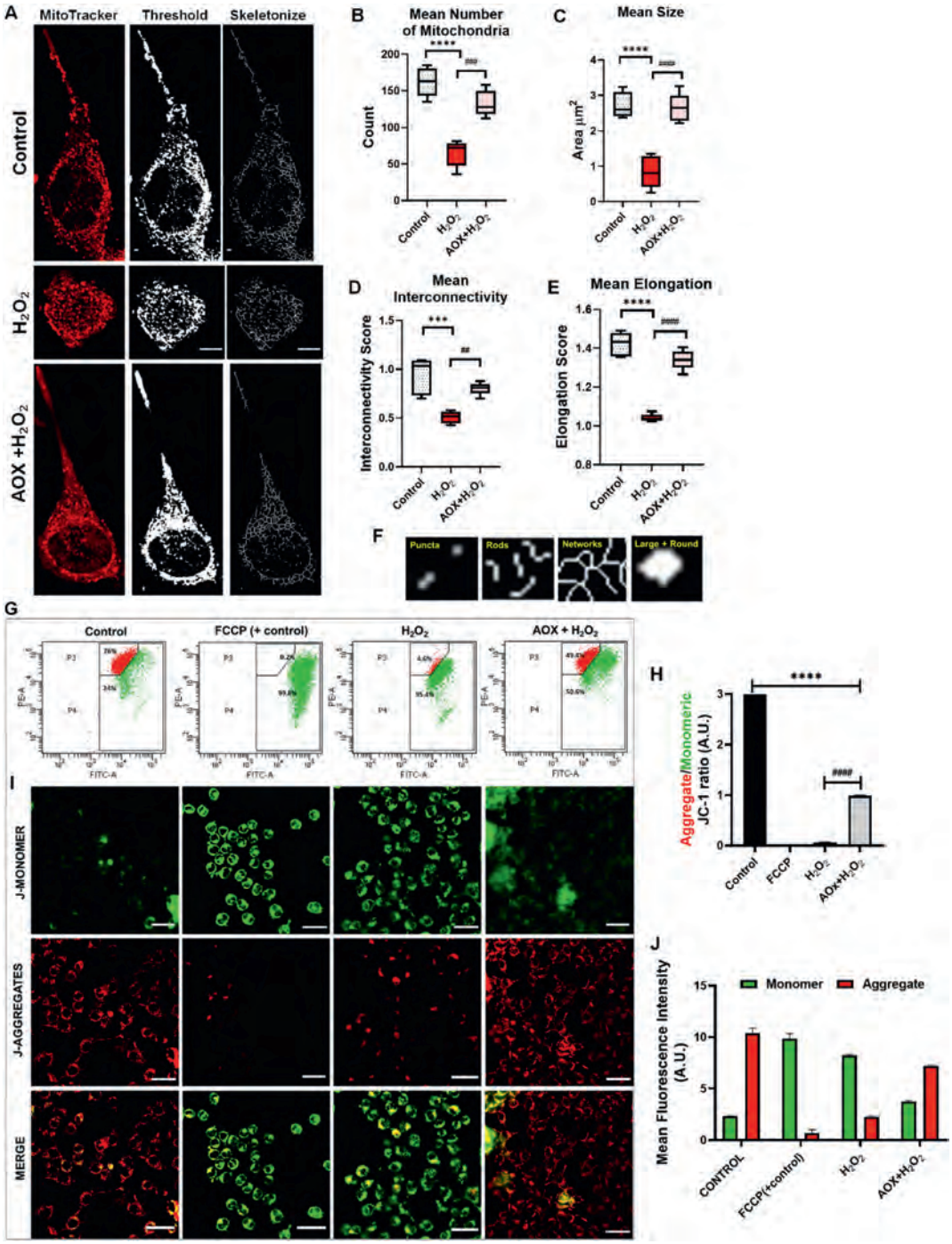

Figure 6 Effects of AOX in mitigating the mitochondrial ROS and maintaining the nito morphology in H_2O_2-induced oxidative stress in dPC12 cells. (A) Visualizing mitochondria and quantifying their morphology: Deconvulated Mitotracker CMX-ROS red stain fluorescence image showing mitochondria with threshold of mitochondrial signal and skeletonized for quantification. Scale bar corresponds to 10 µm. Mitochondrial morphometric measures showing (B) mean number of mitochondria, (C) mean size, (D) mean interconnectivity, (E) mean elongation, (F) classification of 4 mitochondrial morphology subtypes. Mitochondrial membrane potential (MMP, $\Delta\psi_m$) by fluorescent dye JC-1in control, FCCP (+control), H_2O_2, and AOX + H_2O_2 by flow cytometry (G) and by Fluorescence imaging (I). Scale Bar corresponds to 50 µm. (H−J) Quantification of red and green fluorescence intensity was normalized by control. The results are represented as the mean ± SEM. $n = 3$ per group. $^{****}P < 0.0001$ *versus* the control group, $^{\#\#\#\#}P < 0.0001$ *versus* the H_2O_2 group. Data were analyzed using a one-way analysis of variance.

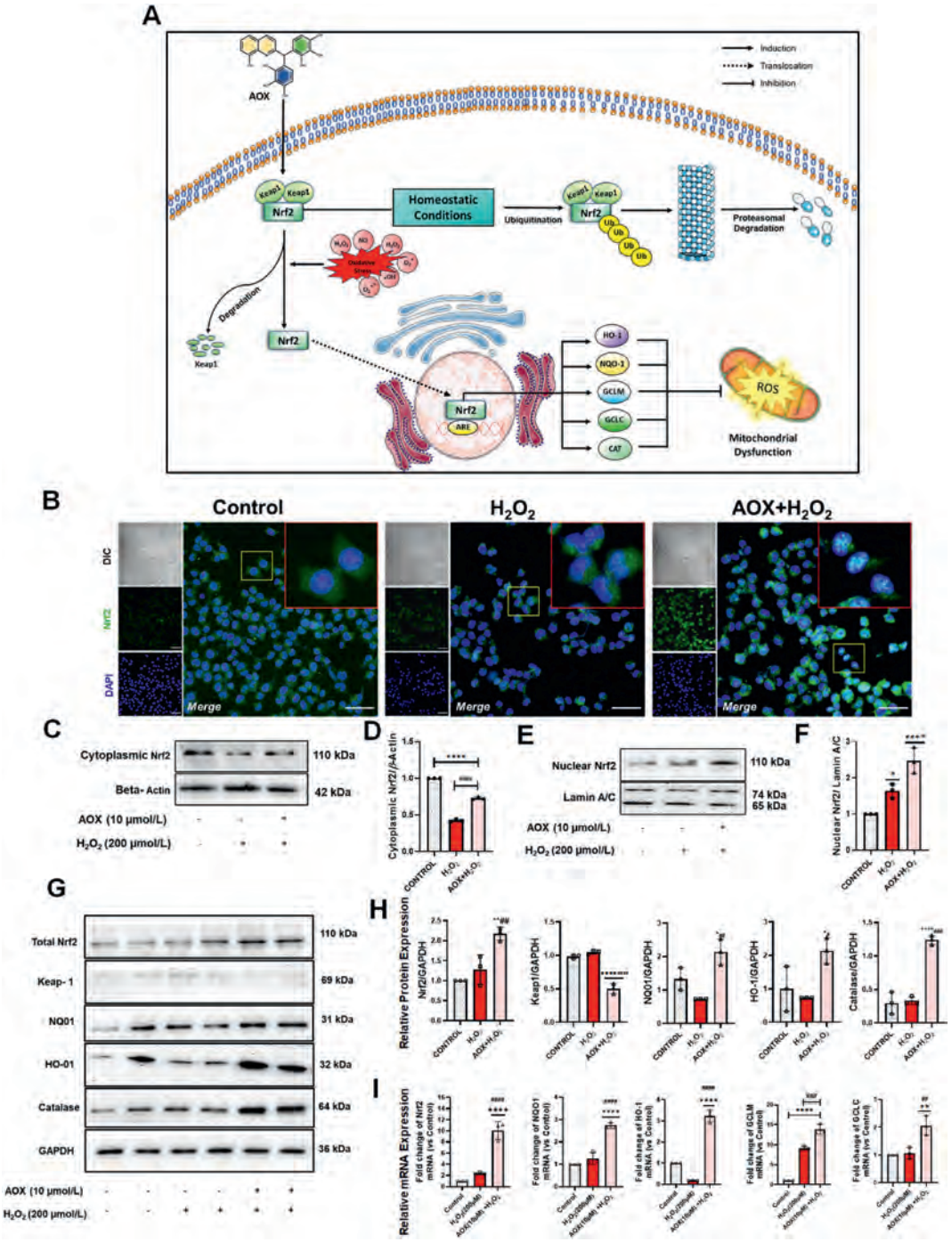

Figure 7 Determining the mechanism of action of AOX in alleviating the ROS through Nrf2/ARE signaling pathway. (A) Schematic representation showing the neuroprotective mechanism of AOX by attenuating H_2O_2-induced oxidative stress in dPC12 cells by activating the Nrf2/ARE signaling pathway. (B) Immunofluorescence staining with anti-Nrf2 (C, E) Expression of Nrf2 protein in both cytoplasm and nucleus. Where, Beta-actin and Lamin A/C serve as the housekeeping protein in Western blot assay for cytoplasmic and nuclear protein respectively. (D, F) Quantitative analysis data. (G, H) The effect of AOX on protein expression of total NrF2, Keap-1, NQO1, HO-1, catalase, and GAPDH was determined by Western blot analysis. (I) Effect of AOX on mRNA expression of total Nrf2, NQO1, HO-1, GCLM, GCLC, and GAPDH in dPC12 cells control and H_2O_2 treatment group assessed using RT-PCR. Data were analyzed using one-way analysis of variance. The results are represented as the mean ± SEM. $n = 3$ per group. $^{*}P < 0.1$, $^{**}P < 0.01$, $^{***}P < 0.001$, $^{****}P < 0.0001$ *versus* the control group, $^{\#}P < 0.1$, $^{\#\#}P < 0.01$, $^{\#\#\#}P < 0.001$, $^{\#\#\#\#}P < 0.0001$ *versus* the H_2O_2 group. Data were analyzed using a one-way analysis of variance. Scale bar corresponds to 50 μm.

2.9. *Exploring AOX treatment outcomes: in vivo investigation of neuroprotective effects in transient bilateral common carotid artery occlusion*

In biomedical research, transitioning from laboratory-based *in vitro* experiments to *in vivo* studies is essential for evaluating the potential of therapeutic candidates in real-world physiological settings. This manuscript outlines our methodological approach to bridging this crucial gap, focusing on assessing the viability and stability of a newly developed antioxidant compound. Antioxidants are of particular interest due to their potential neuroprotective properties in conditions such as neurodegenerative diseases and ischemic stroke. While many antioxidants have shown promise in controlled laboratory environments, their effectiveness in living organisms requires rigorous validation. Our methodology involves a multi-step process, beginning with *in vitro* cell viability assays to assess the compound's ability to protect neuronal cells from oxidative stress. We then progress to optimizing subsequent animal studies in ischemic stroke models allow us to evaluate the compound's ability to cross the blood−brain barrier and mitigate neuronal injury. Our results demonstrate robust neuroprotective effects *in vivo*, culminating in significant protection against ischemic stroke-induced neuronal damage. This comprehensive approach underscores the importance of assessing therapeutic candidates in physiological conditions and provides promising evidence for the translational potential of our antioxidant compound. To perform *in vivo* experiments after the successful activity of AOX *in vitro* assays, it was crucial to ensure that our novel small molecule had good viability in physiological conditions and had the potential to reach the brain and remain stable in the bloodstream. We conducted a BBB crossing experiment by a well-established protocol to assess AOX's ability to cross BBB[51]. The rats were sacrificed here by transcardial perfusion 6 h after the small molecule (0.5 mg/kg) was intraperitoneally administered. The obtained brains were homogenised in acetonitrile solution. Then, HRMS-mass spectroscopy was used to examine the homogenised solutions. The molecular mass peak of our small molecule was visible in the mass spectrum (Supporting Information Fig. S28A). When sucrose was employed as a negative reference, the molecular peak could not be seen in the mass spectrum[51]. This BBB crossing assay demonstrates our small molecule is crossing the BBB and has strong biostability, which suggests that they have a better potential for use in the development of antioxidant drugs. In many applications, including clinical diagnosis, drug development, medical research, and sample storage, serum stability is essential. The accuracy and reliability of experimental outcomes depend on serum stability, which is crucial in medical research. The quantities of important analytes or biomolecules may fluctuate in serum samples because of degradation, denaturation, or chemical alteration. This could lead to false-positive or false-negative findings, which might lead to inaccurate interpretations and resource wastage. Serum stability is crucial for drug development since it has an impact on a dosage pharmacokinetic. We examined the stability of AOX in serum and determined its half-life *in vivo*. AOX was exposed to human serum to evaluate its stability, whereas for the calculation of its half-life, AOX was injected intravenously, and samples were gathered at different time intervals for examination. The stability of AOX in human serum over a 24-h period and its half-life *in vivo* over 24 h were assessed using reversed-phase high-performance liquid chromatography (RP-HPLC). The analysis of the chromatographic results revealed that AOX demonstrated 85.75% stability in human serum for a duration of 24 h, and half-life of 3.31 h approximately (Fig. S28B and S28C). The results indicate that AOX remains stable in serum, showing very little degradation even after being incubated for a lengthy period of time. The strong serum stability and prolonged half-life indicate that AOX has the potential to provide long-lasting therapeutic effectiveness and widespread dispersion throughout the body after being administered.

We then quantified tissue distribution of AOX using RP-HPLC analysis in male Wistar rats administered with an intravenous dose of 0.5 mg/kg. At 0.5, 1, 4, 8, and 24 h post-administration, the concentrations of AOX in the liver, kidney, heart, brain, and lungs were measured. The liver exhibited the highest concentration of AOX, indicative of significant hepatic uptake and metabolism, followed by the lungs and kidneys, which showed moderate levels, suggesting pulmonary distribution and renal elimination (Fig. S28D and S28E). The heart and brain had lower concentrations, reflecting limited penetration into cardiac and cerebral tissues. The high hepatic concentration aligns with the liver role in drug detoxification, while the kidneys significant levels highlight renal excretion. The substantial pulmonary presence suggests the lungs as a secondary site of distribution. Lower cardiac concentrations imply minimal direct effects on the heart, which is beneficial for drugs targeting peripheral sites. Notably, the brain exhibited lower yet consistent concentrations, suggesting a neuroprotective ability of AOX, as its presence, even at low levels, indicates it can cross the blood−brain barrier to exert protective effects without causing significant central nervous system side effects. These results provide crucial insights into AOX's pharmacokinetics and tissue-specific accumulation, guiding its therapeutic application and predicting potential side effects.

Following successful validation of the antioxidant small molecule for BBB crossing and serum stability, an *in vivo* ischemic stroke model induced by transient bilateral common carotid artery occlusion (tBCCAO) is used to simulate cerebral ischemia model to generate the process of ischemic−reperfusion in stroke; mimicking conditions relevant to ischemic stroke. During the procedure, temporary interruption of blood flow to the brain was induced by occluding the common carotid arteries, allowing for a controlled period (20 min) followed by 24 h reperfusion to generate ischemic stroke (Fig. 8A). The duration and severity of the occlusion play a critical role in assessing the molecule's efficacy in mitigating ischemic damage. Studies show that ROS is generated to a small extent during ischemia but the level of ROS is produced rapidly once oxygen is reintroduced during reperfusion. Therefore, to scavenge the excess ROS produced during reperfusion we designed our experiment in such a manner that just after the occlusion our small molecule was injected intraperitoneally at the dose of 0.5 mg/kg body weight to facilitate the scavenging process and display the antioxidant activity by lowering the detrimental effect caused by the tBCCAO/R surgery. Additionally, neurobehavioral assessments and histological analyses of brain tissues were conducted to evaluate AOX's impact on neurological outcomes and potential neuroprotective effects (Fig. 8B). This model is used to study the damage associated with white and gray matter resulting after the reperfusion and the associated abnormalities and damage to the myelin and axons in the optic nerve, optic tract, and as well as caudate putamen which progresses towards the cortex. This surgery led to the drooping of the eyelids after the period of 24 h reperfusion. To our surprise, we noticed minute or no drooping in the treated group and the results were the same for all the 9 animals used for the study (Fig. 8C). To further explore the brain protection with our small molecule we conducted the modified neurological severity

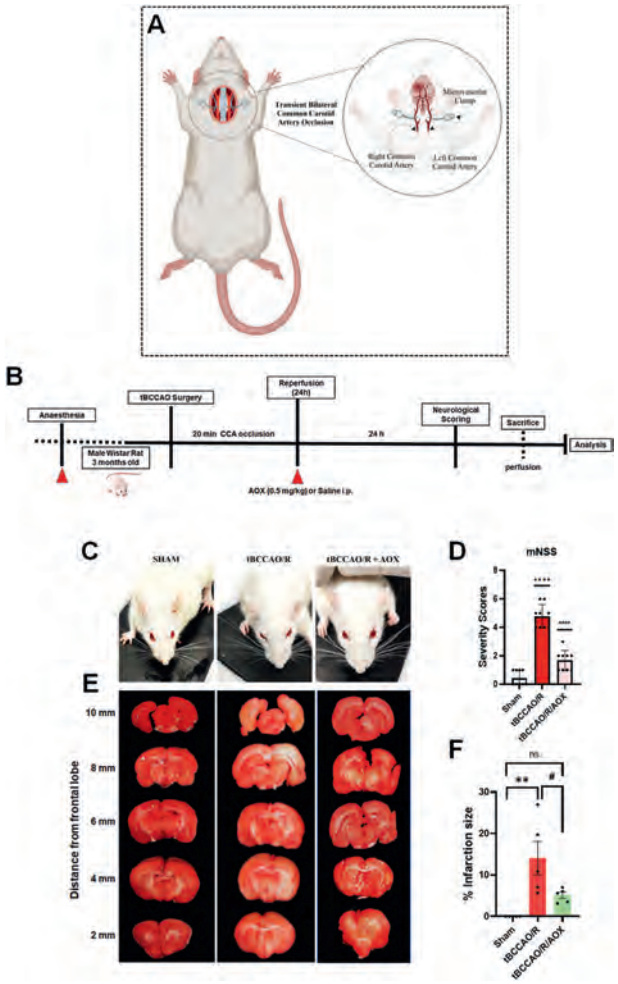

Figure 8 Effect of AOX in tBCCAO/R rat model of stroke. (A) tBCCAO Procedure (B) Experimental timeline for the tBCCAO model Wistar rat and AOX treatment. (C) The physical appearance of the rats after the surgery in sham, tBCCAO/R, and tBCCAO/R + AOX groups with eye drooping in the tBCCAO group had no significant effect in AOX treatment ensuring good antioxidative activity. (D) modified Neurological Severity Scoring (mNSS) on 14 scores based on neurological conditions. (E) TTC staining of 5 consecutive brain slices of all the three experimental groups to detect the infarct location and its volume. (F) Infarct volume percentage was calculated from the TTC brain slice images. The results are represented as $n = 3$ in each group and were analyzed by one-way ANOVA. $^{**}P < 0.01$, $^{****}P < 0.0001$ *versus* sham group $^{\#\#\#\#}P < 0.0001$ *versus* the tBCCAO/R group.

score (mNSS) by Bederson's scoring system to evaluate the neurological condition after the reperfusion period as compared to the saline group. The test was based on sensory, motor, and balance with a total score of 14. The animals were scored accordingly as stated in the scoring system. The higher the score the greater the severity of neurological damage. The results showed that treatments with AOX effectively improved the function and behaviour of tBCCAO/R rats compared to the saline group (Fig. 8D).

The location of the ischemic foci was detected with 2,3,5-triphenyltetrazolium Chloride (TTC) stain showing the infarct area around the cortex and striatum (Fig. 8E). Infarct size was evaluated from TTC-stained five consecutive rat brain slices measuring 2 mm per slice cut using a rat brain matrix. The experimental animals were sacrificed for TTC stain after 24 h of reperfusion which delineates the cerebral infarct area [52]. The brain slices when immersed in the TTC solution stain viable tissue deep red whereas the dead tissue or the infarcted area was left unstained. The sham group rats' brain slices were stained in deep red as they did not undergo the ischemic stroke whereas the tBCCAO/R group rat brain slice showed a demarcated infarct area in the cortex and striatum region accounting for a total infarct volume of 199 mm^3. Whereas in the treatment group (tBCCAO/R/AOX) AOX molecule was injected at the time of reperfusion at a dose of 0.5 mg/kg which showed a significant reduction in the infarct volume which was 80.8 mm^3. The infarct size and area in all experimental groups is listed in Fig. 8F and Table 2, respectively.

2.10. Histomorphological analysis of ischemic brain injury and AOX mediated protection: HE and nissl stains

After 24 h of reperfusion, we elucidated the pathomorphological changes observed in the cortex and striatum region of the brain to analyse the neuroprotective capacity by AOX. The histological brain sections stained with haematoxylin and eosin (HE) of the cortex and striatum region were studied as the stroke area was confirmed through TTC stain. On microscopic examination, we can see the thinness and weak staining of the neuropil with more vacuolization. The emergence of larger, shrunken neurons with pyknosis in their nuclei and eosin-stained cytolymph that was clearly visible was prominent in the infarction area, while AOX reduced the number of pyknotic neurons as well as the area of necrosis (Fig. 9A and B). For the more precise study of the neuronal health, we also examined the damage that occurred to the neurons in the infarcted area using Nissl staining. As shown in Fig. 9C and D compared with the sham-operated control group the number of intact neurons was drastically reduced and also exhibited distorted morphology (Fig. 9E and F). However, in the treatment group, the neuronal damage decreased. These findings also show that AOX efficiently prevents neuronal damage and apoptosis, which lessens the further oxidative damage brought on by ischemia-reperfusion stroke.

2.11. GFAP and S100β expression patterns in ischemic brain injury: assessing AOX protection via comprehensive IHC study

In the reperfusion period, the tissue damage is observed related to the sudden blood flow to ischemic tissue. S100β, a calcium-binding protein B is primarily found in astrocytic glial cells. Mainly astrocytes dendritic cells maturing oligodendrocytes and Schwann cells. S100β expression is involved with the inflammatory process and plays a vital role in the pathogenesis of the brain undergoing ischemic/reperfusion. In this study, we noticed that AOX improved the neurological deficit score and the brain infarct size. The expression of S100β is associated positively with the total infarct size and is reduced with its treatment as compared to the ischemic stroke model (Fig. 10A–C). Resting astrocytes are star-shaped cells with hairlike projections radiating from their cell body whereas the reactive astrocytes in response to any insult get broader in projections. When visualized by antibody against intermediate filament protein GFAP, the projections in the ischemic stroke brain seemed to be thicker and appear longer. Therefore, these morphological changes were seen in tBCCAO/R and tBCCAO/R + AOX treated brain which helps us understand the

Table 1 Primer sequences used for RT-qPCR.

Gene	Forward 5′−3′	Reverse 5′−3′	Accession No.
Nrf2	GGTTGCCCACATTCCCAAAC	ATCCAGGGCAAGCGACTCAT	NM_031789.3
NQO1	AAACGACATCACAGGGGAGC	GGGCACCCCAAACCAATACA	NM_017000.3
HMOX-1	CTAAGACCGCCTTCCTGCTC	GGTAGTATCCTGGGCTCTAAGG	XM_039097469.1
GCLC	GCAGCTCTTAGAGGAAGTGTGA	GGCACTGGTGTGGACCTAGA	XM_039080870.1
GCLM	CCCTGATTTGGTCAGGGAGTTT	GTCCAGCTGTGCAACTCCAA	NM_017305.2
GAPDH	CTCCAACCCAACCCTCAACAG	CCGATACGGCCAAATCCGTTC	XM_039107008.1

Table 2 Infarct size evaluation by 2,3,5-triphenyltetrazolium chloride (TTC) staining.

Group	Brain slice area (mm^2)	Total infarct area (mm^2) (Cortex + Striatum)	Total infarct volume (mm^3) (10 mm (2 mm*5 slice) *Total infarct area (mm^2))	% Infarct size
Sham $n = 5$	141.94 ± 13.92	0	0	0
tBCCAO/R $n = 5$	141.62 ± 2.78	19.9 ± 12.61	199 ± 12.61	14.05
tBCCAO/R/AOX $n = 5$	160.08 ± 10.38	8.08 ± 2.81	80.8 ± 2.81	5.05

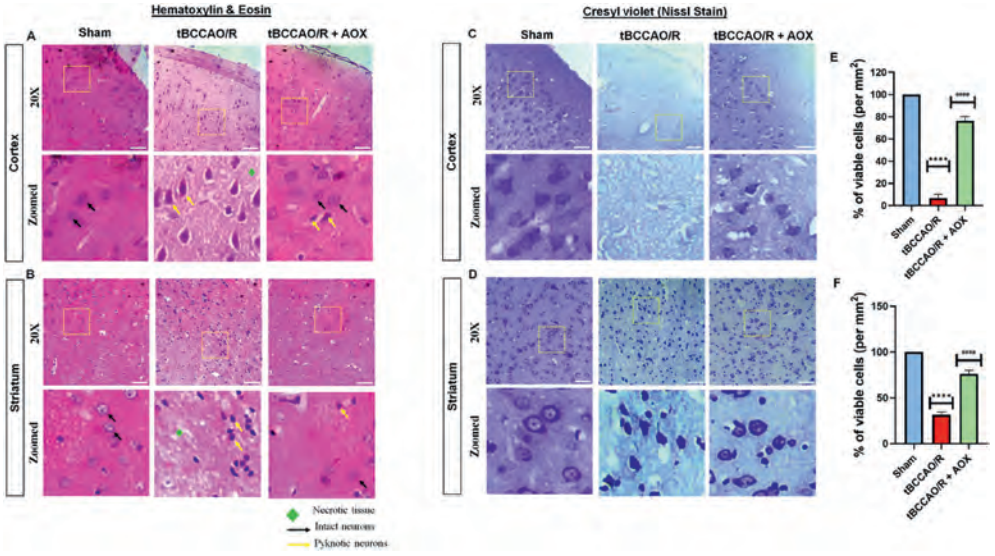

Figure 9 Representative images of Haematoxylin and eosin-stained cells in (A) Cortex and (B) Striatum. Wistar rats were subjected to sham operation in one group, in the tBCCAO/R group rats were subjected to 20 min of ischemia followed by 24 h of reperfusion with the administration of vehicle (saline) and in tBCCAO/R + AOX group AOX (0.5 mg/kg) was injected at the end of ischemia and the start of reperfusion. AOX treatment at the time of reperfusion reduces brain damage after 24 h of tBCCAO ischemic/reperfusion in animals and improves the number of surviving neurons compared to the tBCCAO/R group. Haematoxylin and eosin stain shows massive shrunken neurons with nuclei pyknosis and prominently-stained cytolymph by eosin in 20 × magnification of paraffin embedded brain tissue 5 μm brain section. Representative images of cresyl violet stained cells in (C) cortex and (D) striatum. The morphology of the neuron in the cortex and striatum region visualized with nissl stain and necrotic neurons is visible in the tBCCAO group with significantly increased viable neurons in the treated group. Quantification of the percentage of surviving neurons per mm^2 in (E) cortex and (F) striatum was determined. The results are represented as $n = 3$ in each group and were analyzed by one-way ANOVA. $^{**}P < 0.01$, $^{****}P < 0.0001$ *versus* sham group $^{\#\#\#\#}P < 0.0001$ *versus* the tBCCAO/R group. The scale bar corresponds to 200 μm.

cellular changes in the rat brain after the ischemic stroke (Fig. 10D−F). Astrogliosis increases neuroprotection and releases trophic factors to support the degenerating neurons by forming a glial scar around the damaged area and isolating it from the rest of the CNS tissue. The lesioned area is populated by reactive astrocytes and it's known that it has the property of stem cells. This helps the damaged area to heal by remodeling the brain circuits. The overall result of these functional reactions is beneficial for the nervous tissue.

2.12. Unveiling microglia response: IBA1 expression and morphological changes in ischemic brain injury and protection by AOX

Microglia are resident immune surveillance cells of the brain that constitute about 0.5%−16.6% of human brain cells[53] and 5%−12% of mouse brains[54]. These cells react to the change in the environment by changing its morphology which is used to measure neuroinflammation and pathology. Microglia have a unique

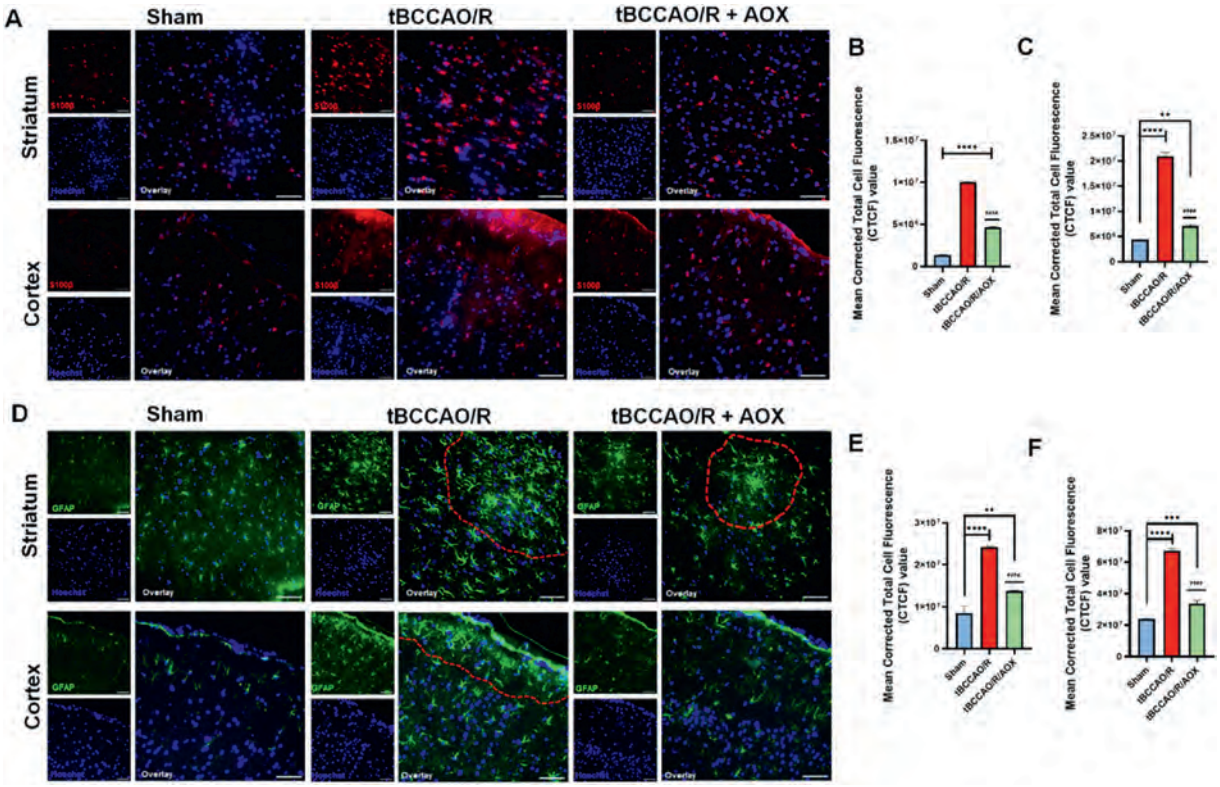

Figure 10 Immunofluorescence staining for S100β in the Striatum and Cortex of Wistar rats given AOX treatment at the time of reperfusion (24 h) (A) Immunofluorescence for in the striatum and cortex. Red fluorescence indicates S100β and blue fluorescence indicates Hoechst. Quantification of S100β expression by calculating mean CTCF value for striatum (B)and cortex (C). Immunofluorescence staining for GFAP in the Striatum and Cortex of Wistar rats given AOX treatment at the time of reperfusion (24 h). (D) Immunofluorescence for GFAP in the striatum and cortex. Green fluorescence indicates GFAP and blue fluorescence indicates Hoechst. The red demarcated dashed lines (−−−−) represent the area with glial scar formation. The quantification of GFAP expression by calculating mean CTCF value for striatum (E)and cortex (F). The scale bar corresponds to 50 μm. $n = 3$ in each group were analyzed by one-way ANOVA. $^{**}P < 0.01$, $^{***}P < 0.001$, $^{****}P < 0.0001$ *versus* sham group $^{\#\#\#\#}P < 0.0001$ *versus* the tBCCAO/R group.

highly ramified shape with numerous sinuous branches originating from a small cell body during non-inflammatory conditions. Microglia quickly alter their shape by shortening their processes and expanding their cell bodies upon detecting any inflammatory or pathogenic stimulation[55]. They even become amoeboid in more severe conditions where necrotic death is seen[56]. Microglia survey and perform synapse pruning and even phagocytose the non-functional neurons as well as synapses. Since disease severity is correlated with morphological alterations in microglia, immuno-histochemical investigations that disclosed the morphology of microglia and the degree of inflammation resulting from tBCCAO surgery were studied.

Ionized calcium-binding adapter molecule 1 (IBA1) is a commonly used microglial reactivity morphological changes marker. In a 40 × immunofluorescence image skeleton analysis was done to compute the average number of branches, branch endpoints, and branch length (Fig. 11A and F).

Furthermore, we quantified microglial morphology at the single-cell level and isolated individual, randomly selected microglial cells from an image in ImageJ using three different single-cell microglia. The spatial complexity of the individually isolated microglia was measured using fractal and lacunarity analysis to determine the complexity and shape heterogeneity of the microglia to calculate the cell density, span ratio, and circularity of the cells which gives the information on the size, elongation, and shape of the cell boundaries respectively[57]. Fractal analysis showed that the microglia in the tBCCAO/R group had a simpler branching pattern, larger cell bodies, fewer and shorter branches, and fewer endpoints than control the microglia in the sham group, while the treatment group's microglia morphology was similar to the sham groups in both cortex and striatum (Fig. 11B, C, G and H). However, differences in lacunarity, circularity, span ratio, and density between sham, tBCCAO/R, and treatment groups were not detected (Supporting Information Fig. S29A−S29E). Sholl analysis was used to assess how far single microglia has branched, using intercepts on concentric circles surrounding the cell body. The microglial ramification was measured by single-cell skeletal analysis showing that the microglia of the tBCCAO group had fewer and less expansive branches than a sham and treatment group (Fig. 11D, E, I and J).

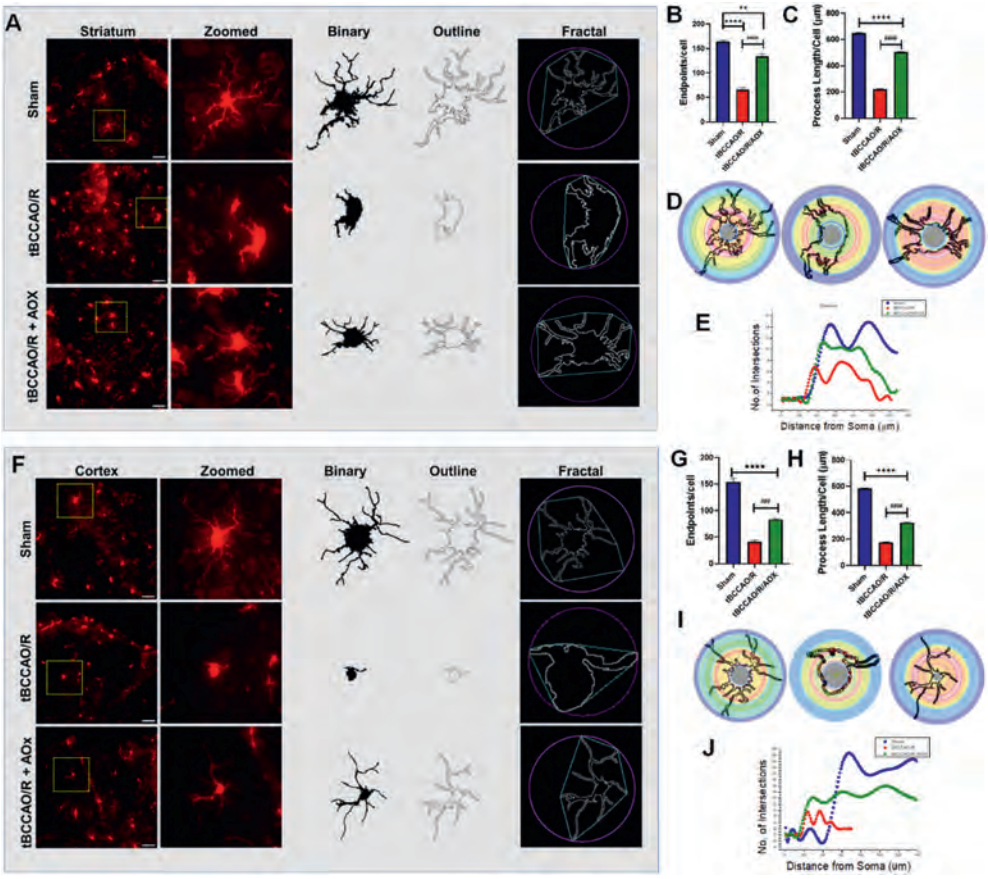

Figure 11 Single-cell assessment of microglial morphology before and after AOX treatment. (A, F) Immunofluorescence staining for IBA1 in the Striatum and Cortex with single cell binary isolated microglia subjected to fractal analysis and converted to outlines and analyzed using the FracLac plugin. Quantitative data of endpoints and process length calculated from fractal analysis for single cell microglia isolated from striatum (B, C) and cortex (G, H) photomicrograph. Sholl analysis was performed to measure cell branching using concentric circles for the striatum (D, E) and cortex (I, J). The scale bar corresponds to 50 µm. $n = 3$ in each group were analyzed by one-way ANOVA. $^{**}P < 0.01$, $^{***}P < 0.001$, $^{****}P < 0.0001$ *versus* sham group $^{\#\#\#\#}P < 0.0001$ *versus* the tBCCAO/R group.

3. Conclusions

In summary, the development of a multifunctional novel 8-HQ-based polyphenolic antioxidants holds immense promise in the realm of neuroprotection and the treatment of neurodegenerative diseases. Pre-treatment with a novel antioxidant small molecule, AOX, showed the antioxidant potential in PC12-derived neurons in H_2O_2 induced oxidative stress cellular model and Wistar rats with induced ischemic stroke, i.p. injection of AOX at the time of reperfusion significantly decreased infarct volume and ameliorated neurological impairments with minimal alterations in neuroinflammatory markers such as GFAP, IBA1 and S100β. Overall, combining two antioxidants and a metal chelator in one small molecule can provide a powerful tool for protecting cells and tissues from oxidative damage, which has been implicated in a wide range of diseases, including cancer, heart disease, and neurodegenerative disorders. Research in this field is ongoing, and scientists are continually working on the development of small molecules that can effectively target and modulate the Nrf2/ARE pathway for therapeutic purposes. Such molecules have the potential to contribute to the treatment and prevention of various diseases related to oxidative stress.

4. Experimental

4.1. Chemicals and reagents

2-Methyl-8-quinolinol is obtained from TCI. 1,2,3-Trimethoxybenzene, Polyphosphoric acid, SeO_2, BBr_3, 1,1,1,3,3,3-hexafluoro-2-propanol, ABTS, DPPH were purchased from Sigma. Dichloromethane (DCM), zinc acetate, sodium bicarbonate, hydrogen peroxide (H_2O_2), NH_4OH, ethyl acetate, *n*-hexane, CCA, Thioflavin-T (ThT), and DCFDA were purchased from Merck (Germany). Horse Serum was bought from Himedia. Rabbit monoclonal antibody, and penicillin−streptomycin were bought from Invitrogen. Copper chloride, zinc chloride, manganese chloride, magnesium chloride, cobalt chloride, nickel chloride, iron chloride, and calcium chloride were bought from SRL. Amyloid beta (1−42) was obtained from Alexotec (Sweden). Nitrocellulose membranes were procured from Merck Millipore. All chemicals were used without purification. Dulbecco's modified Eagle's medium (DMEM-low glucose), horse serum (HS), fetal bovine serum (FBS), bovine serum albumin (BSA), trypsin−EDTA solution, 4′,6-diamidino-2-phenylindole dihydrochloride (DAPI), 3-(4,5-dimethylthiazol-2-yl)-2,5-diphenyltetrazolium bromide (MTT),

formaldehyde solution for molecular biology, penicillin streptomycin solution, dimethyl sulfoxide (DMSO), Bisbenzimide H33258 (HOECHST), Triton X-100 detergent, DPX Mountant, Tween 20 detergent, glycine, Tris base, protease inhibitor, phosphatase inhibitor, RIPA lysis buffer, 2-mercaptoethanol, ammonium persulfate, TEMED, acrylamide/bis-acrylamide solution, sodium dodecyl sulfate (SDS), bromophenol blue, glycerol, methanol, Trizol reagent, nuclease free water, SYBR GREEN PCR Master Mix, Verso cDNA synthesis kit, Immobilon Western HRP substrate, 3color pre-stained protein ladder, PVDF membrane (Millipore), primers were purchased from GCC Biotech, 2,3,5-triphenyltetrazolium chloride (TTC).

4.2. Synthesis of AOX

SeO_2 (30 mmol, 3.33 g) in 1.4-dioxane (50 mL) was taken and to this 1 mL of water was added, then the mixture was heated to 60 °C. 2-Methylquinolin-8-ol (2.39 g, 15 mmol) in 1.4-dioxane (20 mL) was taken and added to the previous SeO_2 solution dropwise over 30 min. The reaction solution was reflux for 12 h at 110 °C. After completion of the reaction, the precipitate was filtered and the filtrate was concentrated using a vacuum. The crude product was purified by silica gel chromatography using ethyl acetate/*n*-hexane, 1:5 to give 2.38 g of the pure title compound as yellow solid[58,59], 92% yield; ^{1}H NMR (400 MHz, DMSO-d_6) δ (ppm) 10.08 (s, 1H), 8.40 (d, J = 8.4 Hz, 1H), 7.87 (d, J = 8.4 Hz, 1H), 7.54 (t, J = 7.8 Hz, 1H), 7.41 (d, J = 8.0 Hz, 1H), 7.16 (d, J = 8.0 Hz, 1H). ^{13}C NMR (100 MHz, DMSO-d_6) δ (ppm) 194.20, 154.79, 150.82, 138.71, 138.15, 131.18, 128.09, 118.44, 117.82, 113.18. HRMS (ESI) calculated for $C_{10}H_7NO_2$ [*m*/*z*]:173.0477, found: 174.0559.

There are three step reaction. The stepwise yield of the step-1 is 92%, step-2 is 77% and step-3 is 74%. Thus, the overall yield (%)= (0.92 × 0.77 × 0.74) × 100 = 52%.

4.2.1. 2-(Bis(2,3,4-tri methoxyphenyl) methyl) quinoline-8-ol (Intermediate-2)

2 g polyphosphoric acid (PPA) was taken in a round bottom flask and heated to 120 °C. When the viscosity was lost then 8-hydroxyquinoline-2-carbaldehyde (100 mg, 1 equiv.) and 1,2,3-trimethoxybenzene (203 mg, 2.1 equiv.) were mixed well and added to PPA with continuous stirring. The solution got red color after some time. After 5 min of continuous stirring ice water was added to the round bottom flask with continuous stirring. Then the solution was neutralized with NH_4OH. The white precipitate was filtered out and dissolved in ethyl acetate. The crude was purified by silica gel chromatography using 20% ethyl acetate−hexane to give 219 mg of a pure compound, 77% yield. ^{1}H NMR (300 MHz, DMSO-d_6) δ (ppm) 8.06 (d, J = 8.4 Hz, 1H), 7.42−7.27 (m, 4H), 7.11 (d, J = 7.5 Hz, 1H), 6.60 (d, J = 8.7 Hz, 2H), 6.57 (d, J = 8.7 Hz, 2H), 6.35 (s, 1H), 3.87 (s, 6H), 3.84 (s, 6H), 3.61 (s, 6H). ^{13}C NMR (100 MHz, DMSO-d_6) δ (ppm) 161.76, 152.93, 152.66, 151.54, 142.47, 138.30, 136.83, 129.19, 127.67, 127.38, 124.49, 122.74, 118.21, 111.60, 111.05, 107.86, 60.77, 60.72, 56.23, 46.52. HRMS (ESI) calculated for $C_{28}H_{29}NO_7$ [*m*/*z*]: 419.1944, found: 412.2027.

4.2.2. 4,4′-((8-Hydroxyquinoline-2-yl) methylene) bis(benzene-1,2,3-triol) (AOX)

100 mg of 2-(Bis(2,3,4-trimethoxyphenyl) methyl) quinolin-8-ol was mixed with dichloromethane under an inert atmosphere in a round bottom flask and cooled it to −78 °C. After that boron tribromide (BBr_3) in dichloromethane was added to it. After stirring at −78 °C for 2 h, the reaction mixture was allowed to warm to room temperature with continuous stirring for 24 h. After that, it was cooled to 0 °C and added water. Removing the dichloromethane under reduced pressure the mixture was extracted with ethyl acetate. The combined organic layer was reduced under low pressure and the crude product was purified through column chromatography with 10% methanol in dichloromethane to give a 62 mg very light yellow product, a 74% yield[60]. ^{1}H NMR (600 MHz, CD_3OD) δ (ppm) 8.83 (s, 1H), 7.73 (d, J = 8.4 Hz, 1H), 7.68 (t, J = 7.8 Hz, 1H), 7.64 (d, J = 8.4 Hz, 1H), 7.38 (d, J = 7.2 Hz, 1H), 7.30 (d, J = 7.2 Hz, 1H), 6.35 (d, J = 8.4 Hz, 2H), 6.31 (d, J = 8.4 Hz, 2H), 4.57 (s, 1H). ^{13}C NMR (150 MHz, CD_3OD) δ (ppm) 163.05, 145.94, 145.89, 145.31, 144.12, 144.11, 133.24, 129.86, 128.32, 127.90, 126.81, 126.54, 123.28, 119.99, 119.89, 118.43, 115.97, 115.95, 115.82, 106.63, 45.25. HRMS (ESI) calculated for $C_{22}H_{17}NO_7$ [*m*/*z*]: 407.1005, found: 408.1081.

4.3. Preparation of Aβ solution for thioflavin-t assay

Aβ_{42} peptide was dissolved in 1,1,1,3,3,3-hexafluoro-2-propanol to prepare the Aβ_{42} monomers. A fixed amount of solution was taken and was evaporated under the mild flow of N_2 gas to obtain precipitated Aβ_{42} peptide. After that, a minimum amount of DMSO was added to solubilize the Aβ peptide. Then fixed amount of buffer solution was added to get the desired concentration of Aβ.

4.4. Metal ion binding and stoichiometry calculation

The interaction between metal ions and the AOX ligand was measured using UV−vis spectroscopy. The final concentration of AOX was 5 μmol/L. Al^{3+}, Zn^{2+}, Ni^{2+}, Mg^{2+}, Fe^{3+}, Co^{2+}, and Cu^{2+} ions were taken as a metal ion to know the selective interaction. The concentration of the all-metal ions is also 5 μmol/L as a 1:1 binding ratio. Next, the copper titration was performed with AOX (10 μmol/L), increasing the molar concentration of Cu^{2+} from 2.5 μmol/L to 35 μmol/L as a 1:3.5 binding ratio. GraphPad Prism 8.0.2 was used to analyse and plot the data.

4.5. Tyrosine quenching assay

Aβ_{42} (10 μmol/L), and Cu^{2+} (10 μmol/L) in PBS were co-incubated with and without AOX (10 μmol/L). For control, fresh Aβ_{42} (10 μmol/L) peptide solution was taken. Fluorescence of the solution was recorded by exciting the solution at 285 nm in Quanta Master spectrofluorometer (QM-40) using a slit width of 1.25 nm. The emission was noted from 295 to 400 nm and the wavelength emission maxima was 308 nm. Finally, the graph was plotted using GraphPad Prism software.

4.6. Bradford assay for monitoring copper-independent and copper-dependent Aβ42 fibrillation inhibition

For studying the copper-independent Aβ_{42} fibrillation PBS buffer (pH 7.4) was used to dilute the Aβ_{42}. For Aβ_{42} aggregates, only Aβ_{42} (10 μmol/L) was vortexed for 72 h at 37 °C. In other cases, AOX was added by 0.5, 1, 2, 5, and 10 μmol/L along with Aβ_{42} and incubated similarly. After 72 h incubation, this solution was centrifuged at 12000 rpm and the filtrate of this mixture was taken. Bradford reagents were added to this solution and the absorbance of the solution was measured by using microplate reader at 595 nm.

Similarly, for copper-dependent Aβ_{42} fibrilization PBS buffer (pH 7.4) was used to dilute the Aβ_{42}. For copper-dependent Aβ_{42} aggregates, Aβ_{42} (10 μmol/L) and Cu^{2+} (10 μmol/L) was incubated for 72 h at 37 °C with agitation. In other cases, AOX was added by 0.5, 1, 2, 5, and 10 μmol/L along with Aβ_{42} and copper and incubated similarly. After 72 h incubation, this solution was centrifuged at 12,000 rpm and the filtrate of this mixture was taken. For control, a fresh Aβ_{42} peptide solution was taken. Next, Bradford reagents were added to this solution and the absorbance of the solution was measured by using microplate reader at 595 nm and the graph was plotted using GraphPad Prism software.

4.7. Thioflavin-T assay for monitoring copper independent Aβ42 fibrillation inhibition

For reading the copper-independent Aβ_{42} fibrillation PBS buffer (pH 7.4) was used to dilute the Aβ_{42}. For the control experiment, only Aβ_{42} (10 μmol/L) was vortexed for 72 h at 37 °C. In other cases, AOX was added by 0.5, 1, 2, 5, and 10 μmol/L along with Aβ_{42} and incubated similarly. After 72 h incubation this solution was diluted with PBS and ThT (50 μmol/L) was added. Fluorescence of the final solution was read by exciting the solution at 435 nm in Quanta Master Spectrofluorometer (QM-40) using a slit width of 1.25 nm. The emission was recorded from 445 to 600 nm and the graph was plotted using GraphPad Prism software.

4.8. Thioflavin-T assay for monitoring copper dependent Aβ42 fibrillation inhibition

For reading the copper-dependent Aβ_{42} fibrillation PBS buffer (pH 7.4) was used to dilute the Aβ_{42}. For the control experiment, Aβ_{42} (10 μmol/L) and Cu^{2+} (10 μmol/L) were vortexed for 72 h at 37 °C. In other cases, AOX was added by 0.5, 1, 2, 5, and 10 μmol/L along with Aβ_{42} and copper and incubated similarly. After 72 h incubation this solution was diluted with PBS and ThT (50 μmol/L) was added. The fluorescence was recorded from 445 to 600 nm by exciting at 435 nm and the graph was plotted in GraphPad Prism software.

4.9. Docking study to visualize the interaction

The molecular docking experiment was performed using the reported method[61]. For this docking research, the protein model made use of the frequently used Aβ_{42} peptide (PDB ID 1IYT)[62] and Aβ_{42} fibril structure (PDB ID 5KK3)[63].

4.10. CD spectroscopy

Aβ_{42} (10 μmol/L) and AOX (1, 5 and 10 μmol/L) solution were incubated for 72 h at 37 °C while being constantly shaken. Next, the CD experiment was carried out by using the method[61]. The data were analyzed and plotted by using GraphPad Prism.

4.11. CCA assay

To perform the CCA assay stock solutions for Cu^{2+}, sodium ascorbate, 3-CCA, and AOX, and gallic acid (positive control) were prepared. To read the fluorescence Cu^{2+}, 3-CCA, and ascorbate were added in such a way so that the final concentrations would be 10, 150, and 200 μmol/L respectively. For the treatment of AOX, different concentrations (0.5, 1, 2, 5, and 10 μmol/L) and gallic acid (10 μmol/L) were added. The fluorescence was being read from the very first moment after addition. The wavelength of excitation was 395 nm and of emission 450 nm. The graph was plotted with the help of GraphPad Prism.

4.12. Media stability of AOX

AOX was incubated with PC12 cell culture media to achieve a final concentration of 100 μmol/L at 37 °C. At specified time intervals (0, 2, 6, 12, and 24 h), 100 μL of the incubated solution was withdrawn and diluted with an equal volume of acetonitrile. Subsequently, the diluted solutions were subjected to analysis using RP-HPLC for purity determination. Graphical representation of the obtained data was performed using GraphPad Prism software.

4.13. Serum stability of AOX

AOX was incubated with 50% human serum to keep the final concentration of 150 μmol/L of AOX at 37 °C. 100 μL incubated solution was taken out and diluted with 100 μL of acetonitrile to complete the precipitate of serum proteins at different time intervals (0, 1, 6, 12, and 24 h). Then the solution mixture was kept at 4 °C to stop the protease activities for 20 min. Next, mixtures were taken out and centrifuged at 10,000 rpm for 10 min at 4 °C. The filtrate solution was then taken and analyzed by RP-HPLC purity measurement. The graph was plotted with the help of a GraphPad Prism.

4.14. Half-life of AOX

Half-life of AOX was determined according to the previously reported protocol with some modifications[64,65]. To determine the half-life of AOX, a dosage of 0.5 mg of AOX per kilogram was intravenously delivered through the jugular vein. Blood samples were obtained from the tail vein using a 21−23-gauge needle at different time intervals (3, 6, 12, 18, and 24 h) and collected into BD Vacutainer® PPT™ Plasma Preparation Tubes. The serum that was gathered was immediately separated using centrifugation at a speed of 5000 revolutions per minute for 5 min at room temperature. It was then stored in a frozen state at a temperature of −80 °C until it could be analyzed. The levels of Serum AOX were measured using HPLC analysis conducted with a Shimadzu LC-20AP instrument. The graph was plotted with the help of GraphPad Prism and Excel. The half-life of AOX was determined by Eq. (1):

$$K\text{elim} = \left(\frac{\ln(C\text{peak}) - \ln(C\text{trough})}{T\text{interval}}\right)$$

$$t_{1/2} = \left(\frac{0.693}{K\text{elim}}\right) \quad (1)$$

4.15. Tissue distribution

Tissue distribution of AOX was determined according to the previously reported protocol with some modifications[66]. This study utilized male Wistar rats (200−250 g) acclimated for one week under standard laboratory conditions. AOX was administered intravenously at a dose of 0.5 mg/kg, and rats were euthanized at 0.5, 1, 4, 8, and 24 h post-administration for tissue collection (liver, kidneys, heart, brain, and lung). Tissues were weighed, homogenized in phosphate buffer saline, and extracted

with methanol. The supernatants were collected post-centrifugation for HPLC analysis. Using a C18 column and a mobile phase of water and acetonitrile (60:40) at a 1.0 mL/min flow rate, the detection was performed at 254 nm. Standard solutions of AOX (0.5−50 μg/mL) established a calibration curve correlating concentration to peak area. Tissue extracts were injected into the HPLC under identical conditions, and peak areas were used to determine AOX concentrations (μg/mL) *via* the calibration curve. Data were statistically analyzed to calculate mean concentrations and standard deviations across tissues and time points, illustrating AOX tissue-specific accumulation using GraphPad Prism software.

4.16. DPPH assay

A stock solution of DPPH (100 μmol/L) was prepared in methanol and 500 μL was added to all the tubes followed by 500 μL of AOX at various concentrations (100, 50, 25, 12.5, 6.25, 3.125, 1.562, 0.78, 0.39, 0.19, and 0). Therefore, the final concentration of DPPH becomes 50 μmol/L for each assay and the concentration of AOX becomes 50, 25, 12.5, 6.25, 3.125, 1.562, 0.78,0.39, 0.19, and 0 μmol/L, respectively. The tubes were incubated for 30 min in the dark and after the incubation the absorption was measured at 517 nm using a UV spectrophotometer. The following Eq. (2) was used to determine the % DPPH scavenging activity:

$$\text{DPPH scavenging activity } (\%) = \left(\frac{\text{Absorbance S} - \text{Absorbance C}}{\text{Absorbance B}}\right) \times 100 \quad (2)$$

where Absorbance S is the absorption of the DPPH, and Absorbance C is the absorption of DPPH measured in the presence of AOX.

4.17. ABTS (2,2′-azinobis-(3-ethylbenzothiazoline-6-sulfonic acid) assay

We measured the ABTS radical scavenging activity with a modified version of a previously published protocol[67]. Briefly, the ABTS solution was prepared by mixing an equal volume of 7 mmol/L ABTS with 2.45 mmol/L potassium persulfate. For 12−16 h, this combination was incubated at room temperature in the dark. PBS was added to the solution to dilute it until the absorbance at 734 nm was 0.700. The diluted solution was mixed equally with the sample solution and the mixture was immediately measured at 734 nm using Microplate Reader and data was plotted and analyzed by GraphPad Prism 8.0.2 software. The ABTS radical scavenging activity (%) was calculated as Eq. (3):

$$\text{ABTS scavenging activity} = 1 - \left(\frac{\text{Absorbance S} - \text{Absorbance C}}{\text{Absorbance B}}\right) \times 100 \quad (3)$$

where Absorbance S, Absorbance C, and Absorbance B are the absorbance values of the sample, control, and blank, respectively.

4.18. Nitric oxide assay

Sodium nitroprusside (5 mmol/L) prepared in PBS was used to generate nitric oxide. It was then combined with varying amounts of AOX and standard gallic acid and incubated for 45 min at 37 °C. After incubation 1:1 ratio of solution was diluted with Griess reagent (1:1 ratio of *N*-(1-naphthyl) ethylenediamine: sulphanilic acid, molecular probes-cat #G-7921). The chromophore generated during the diazotization of nitrite with Griess reagent was measured for absorbance at 548 nm. The nitric oxide scavenging percentage was calculated as Eq. (4):

$$\text{Nitric oxide scavenging } \% = 100 - \left(\frac{\text{Absorbance S} - \text{Absorbance B}}{\text{Absorbance C}}\right) \times 100 \quad (4)$$

where Absorbance S, Absorbance C, and Absorbance B are the absorbance values of the sample, control, and blank, respectively.

4.19. DNPH assay (protein oxidation)

Protein oxidation assay was performed using the already described method [48]. Briefly, BSA (1 mg/mL), H_2O_2 (2.5 mmol/L), and Cu^{2+} (0.1 mmol/L) were incubated separately for 24 h in PBS (pH = 7.4) at 37 °C with various concentrations of AOX and Ascorbate. Carbonyl group quantitation of the protein was carried out using DNPH (10 mmol/L in 0.5 mol/L H_3PO_4) and the incubated solution in the ratio of 1:1 and incubated together for 15 min in the dark at 37 °C. The reaction mixture was then incubated at 20 °C with 250 μL of trichloroacetic acid (50%, *w*/*v*) followed by centrifugation for 5 min. Without disturbing the pellet, the supernatant was disposed of, and 1 mL of ethanol/ethyl acetate (1/1, *v*/*v*) was washed three times. After washing the pellet was resuspended in 6 mol/L guanidine-HCl allowing for the measurement of absorbance at 370 nm. The protein oxidation percentage was calculated using Eq. (5):

$$\text{Protein oxidation } \% = \left(\frac{\text{Absorbance C} - \text{Abs}}{\text{Absorbance C}}\right) \times 100 \quad (5)$$

where Abs is the absorption of DNPH and Absorbance C is the absorption of DNPH measured in all the samples and positive control Ascorbate.

4.20. Cell culture and H_2O_2 induced oxidative stress cellular model

Eosinophilic and neuroblastic cells make up the rat pheochromocytoma cell line (PC12). Cells were cultured DMEM supplemented with 10% horse serum, 5% fetal bovine serum (FBS, Gibco, Grand Island, NY, USA), and 1% penicillin/streptomycin and incubated at 37 °C with 5% CO_2 in a humidified incubator. To differentiate PC12 cells into neuron-like cells (dPC12) by causing the cell body to sprout long neurite-like processes it was fed the following day with 50 ng/mL NGF in DMEM supplemented with 1% horse serum and then incubated for 5 days at 37 °C under 5% CO_2 to ensure appropriate differentiation. 50% of the culture medium was replaced with fresh medium every 2 days. All the cellular experiments were carried out using differentiated PC12 (dPC12) cells.

Oxidative stress was induced by incubating the dPC12 cells with various concentrations of oxidant, hydrogen peroxide for 2 h in the incubator to attain approximately 50% cell death.

4.21. Cell viability assay

MTT assay was used to measure cell viability following the previously described method. In brief, PC12 cells were plated at a low density (1×10^4 cells/well) in a 96-well culture plate and cultured for 24 h followed by differentiation the next day. The

dPC12 cells were pre-treated with various concentrations of AOX small molecule and were incubated at 37 °C with a 5% CO_2 environment for 24 h. After appropriate treatments of induction of oxidative stress, the cells were incubated with MTT solution (5 mg/mL) prepared in filtered PBS solution for 4 h. After 4 h the culture media was discarded and the formazan crystal formed was solubilized with DMSO:methanol (1:1) solution. The absorbance was recorded using a multiplate reader at 550 nm. The cell viability percentage was calculated as Eq. (6):

$$\text{Cell viability}\ (\%) = \left(\frac{\text{Absorbance Treatment}}{\text{Absorbance Control}}\right) \times 100 \tag{6}$$

the cell recovery percentage was calculated as Eq. (7):

$$\text{Cell recovery}\ (\%) = \left(\frac{\frac{\text{CV Exp}-\text{CV}}{\text{model}}}{\frac{\text{CV control}-\text{CV}}{\text{model}}}\right) \times 100 \tag{7}$$

where CV Exp is the cell viability of the experimental group, CV model is the cell viability of the H_2O_2 induced oxidative stress group, and CV control is the cell viability of the control group.

4.22. Live dead assay (Calcein-AM/PI)

To study the cell viability effect of AOX on H_2O_2-induced cell damage, a live-dead assay was performed using Calcein-AM and propidium iodide (PI). The four experimental groups of dPC12 cells cultured on confocal dishes were individually treated at a final concentration of AOX (10 μmol/L) for 24 h followed by 2 h treatment with/without H_2O_2 (200 μmol/L). Live cells were analyzed using Calcein-AM, a cell permeate dye. Whereas dead cells with compromised cell membranes were stained with PI. Briefly, a cocktail of the dyes was prepared (Calcein-AM 2 μmol/L + PI 2 μg/mL) in colorless DMEM media and was added to the PBS-washed culture dishes at a volume of 300 μL and incubated in the dark for 5 min at room temperature. After the incubation, the culture dishes were washed with PBS and subjected to live cell imaging under the fluorescence microscope (OLYMPUS IX83) with FITC filter for Calcein-AM which emits green fluorescence, and TRITC filter for PI which emits red fluorescence. Captured fluorescence images were further assessed and quantified for viability percentage using ImageJ software.

4.23. Measurement of lactate dehydrogenase (LDH) release

The amount of LDH released into the medium due to H_2O_2-induced cell injury was performed using Cayman's LDH cytotoxicity assay kit (Item No. 601170) following the manufacturer's instructions. This assay operates by monitoring the enzymatic conversion of lactate to pyruvate by LDH, measuring the associated increase in absorbance at a specific wavelength. For this experiment, PC12 cells were seeded in a 96-well plate at a density of 10,000 cells/well and differentiated into neurons. After that dPC12 cells were pre-treated with AOX at various concentrations (0.0784, 0.1565, 0.3125, 0.625, 1.25, 2.5, 5, and 10 μmol/L) and incubated for 24 h followed by with/without H_2O_2 treatment for 2 h. The % LDH release was evaluated by measuring its activity in the culture medium incubated with LDH reaction solution and incubated on an orbital shaker for 30 min at 37 °C with gentle shaking. Absorbance was taken at 490 nm using a microplate reader (Thermo Scientific; Varioskan Lux). The percentage LDH release was calculated as Eq. (8):

$$\text{LDH release}\ (\%) = \left(\frac{[\text{Experimental value } A_{490}] - [\text{Spontaneous release } A_{490}]}{[\text{Maximun release } A_{490}] - [\text{Spontaneous release } A_{490}]}\right) \times 100 \tag{8}$$

4.24. Assessing antioxidant enzyme activity

The activity of superoxide dismutase (SOD), glutathione (GSH), glutathione peroxidase (GSH-Px), catalase and malondialdehyde (MDA) content was determined by using Cayman Chemical kit (Item Nos. 706002, 703002, 703102, 10009055 and 707002, respectively) following the manufacturer's instructions. Briefly, PC12 cells were seeded in 6 well plates and incubated at 37 °C and 5% CO_2 for 24 h. On 60% confluency, the cells were differentiated with DMEM medium supplemented with 1% horse serum and 100 ng/mL NGF and incubated for 5 days. After the cells were differentiated with visible neurite outgrowth, they were treated with different concentrations of AOX (0.3125, 0.625, 1.25, 2.5, 5, and 10 μmol/L) and incubated for 24 h followed by treatment with oxidant (200 μmol/L H_2O_2) for 2 h. The cells were harvested using a cell scraper rather than using any proteolytic enzymes and collected by centrifugation (2000×g for 10 min at 4 °C). The cell pellets were homogenised with cold RIPA buffer over ice for 10 min. Following the instructions included in the kit, the homogenates were centrifuged at 10,000×g for 15 min at 4 °C. The supernatants were then utilised for the SOD, GSH, GPx, MDA, and Catalase assays using a microplate reader.

4.25. Detection of intracellular reactive oxygen species (ROS)

One of the most used methods for measuring intracellular ROS is the 2′,7′-dichlorodihydrofluorescein diacetate Assay (DCFH-DA). A stock solution of 10 mmol/L DCFDA was prepared in DMSO and a working concentration of 10 μmol/L was freshly prepared in colorless DMEM culture media and used for the assay. Briefly, dPC12 cells were pre-treated with or without various concentrations of (10, 5, 2.5, 1.25, 0.625, 0.312, 0.156, and 0.078 μmol/L) AOX and incubated for 24 h at 37 °C with 5% CO_2 followed by treatment with 200 μmol/L H_2O_2 for further 2 h to generate oxidative stress. To quantify the amount of ROS generated in the cells, a prepared working concentration of DCFDA was added to the cells and incubated for 15 min in the incubator. The cells were then thoroughly washed with PBS buffer and analyzed by fluorescence imaging (Olympus IX83) under 10 × objective, flow cytometry (BD LSR-FORTESA), and microplate reader at an excitation/emission of 485/530 nm wavelength (Thermo Varioskan lux).

4.26. Flow cytometry analysis

Cells were seeded in 6-well culture plates and incubated overnight followed by differentiation for further 5 days. Then the dPC12 cells were pre-treated with novel small molecule followed by a 2 h oxidant treatment(H_2O_2). After that, the cells were

washed to remove any residual culture medium and resuspended in appropriate concentration to stain it with DCFDA and JC-1 solution by the manufacturer's instructions. The stained cells were then analyzed by BD LSR-FORTSEA flow cytometer for the intensity of green fluorescence of DCFDA and red and green fluorescence for JC-1 aggregates and monomers.

4.27. Measurement of cellular oxidative stress in live cells (CellROX)

To measure the intracellular reactive oxygen species (ROS) in live cells a fluorogenic probe CellROX Deep Red Reagent (Invitrogen, C10422) was used according to the instructions of the manufacturer. In brief, PC12 cells were plated in a confocal glass bottom dish (35 mm) and differentiated. After that, dPC12 cells were incubated with the indicated treatment, and the CellROX reagent was added to a final 5 μmol/L concentration and incubated for 30 min at 37 °C. The cells were then washed with PBS and microscopy images were taken using Olympus IX83 fluorescence microscope. The images were analyzed further for the mean fluorescence intensity using ImageJ software.

4.28. Measurement of mitochondrial superoxide ROS (MitoSOX)

Mitochondrial ROS was detected using a fluorescent probe MitoSOX Red mitochondrial superoxide indicator (Invitrogen, M36008) following the manufacturer's instruction. dPC12 cells treated with oxidant and AOX were incubated with a 5 μmol/L working solution of MitoSox prepared in colorless DMEM culture medium for 10 min at 37 °C, protected from light. The cells were washed thrice with warm PBS to remove the probe for visualization under fluorescence microscope (Olympus IX83). Image fluorescence intensity was analysed and quantified using ImageJ software.

4.29. Mitochondrial morphology analysis

The combined use of Hoechst, Phalloidin, and Mitotracker CMXROS staining provides a comprehensive view of unlocking the cell dynamics. These stains shed light on the morphology of mitochondria, the organization of the cytoskeleton, and the nuclear organization within cells. To study the mitochondrial morphology of cells on various treatments the cells were stained with mitoTracker CMXROS red. Briefly, the dPC12 cells were incubated with 200 nmol/L of mitoTracker CMXROS red probe prepared in colourless DMEM for 10 min in the dark. Fluorescence microscopy was used to image the stained mitochondria. Mitochondrial morphology was observed and analyzed using a fluorescence microscope (Olympus IX83) equipped with a 60 × oil immersion objective. The images were analyzed using ImageJ software. After acquiring the images using a fluorescence microscope the images were analyzed for mitochondrial morphology following previously described method[68]. Briefly, an analysis of mitochondrial morphology was performed on MitoTracker CMXROS images. Firstly, the images were subjected to a threshold to make binary images and were skeletonized and the particles were analyzed by the ImageJ software. To determine the four parameters of the mitochondrial morphology the software simply counted each signal and determined the pixel area, perimeter, and circularity for each signal. The following Eqs. 9−11 were done to determine the score of interconnectivity and elongation:

$$\text{Interconnectivity} = \frac{\text{Mean area}}{\text{Mean perimeter}} \tag{9}$$

$$\text{Elongation} = \frac{1}{\text{Circularity}} \tag{10}$$

$$\text{Circularity} = 4 \times \pi \times \left(\frac{\text{Mean area}}{\text{Mean perimeter 2}} \right) \tag{11}$$

4.30. Mitochondrial membrane potential ($\Delta\psi m$) measurement

The changes in mitochondrial membrane potential (MMP) were measured with a JC-1 assay kit (BD Pharmingen Mitoscreen, 551302) according to the manufacturer's instructions. Briefly, cultured and treated dPC12 cells were harvested by trypsinization and collected by centrifugation at 400×*g* for 5 min at RT. The obtained pellet was washed mildly with cold PBS and suspended in 0.5 mL of freshly prepared JC-1 working solution, vortexed to avoid cell-to-cell clumping, and incubated for 15 min in a CO_2 incubator at 37 °C. Subsequently, the cells were washed twice with 1 × assay buffer followed by centrifugation and suspended in 0.5 mL 1 × assay buffer to analyze the cells by flow cytometry (BD LSR-FORTSEA). After the corresponding treatment, the cells were stained with JC-1 as described above and visualised by Olympus IX83 fluorescence microscope. The images were analyzed and quantified using ImageJ software. Thus, the MMP was indicated by the ratio of red (JC-1 aggregate) to green (JC-1 monomer) fluorescence intensity indicating healthy and unhealthy cells respectively.

4.31. Western blotting

PC12 cells were cultured in six-well culture plates and differentiated for further treatments. The dPC12 cells were collected, washed, and lysed with ice-cold RIPA lysis buffer and a 1% (2:1) protease and phosphatase inhibitor cocktail. The total protein isolated was quantified using Bradford assay. Equal amounts of protein samples (40 μg) were separated on a 10% and 12% SDS/PAGE gel and transferred electrophoretically onto a PVDF membrane. Subsequently, the PVDF membrane was blocked with 5% BSA for 2 h and incubated with primary antibody overnight at 4 °C. The membrane was washed thrice with 1 × TBST buffer and incubated with HRP-conjugated secondary antibody for 2 h at RT. Proteins were visualized by exposure in a BIO-RAD ChemiDoc using immobilon forte western HRP substrate. The band density was quantified by Image Lab 6.1 software.

4.32. Immunocytochemistry

PC12 cells were cultured on 35 mm glass-bottom confocal dishes and differentiated as described before. dPC12 cells were pretreated with AOX followed by oxidant as indicated. After the treatment, cells were fixed with 4% formaldehyde solution for 2 h at 37 °C, washed thrice with PBS, and permeabilized with 0.3% Triton X-100 containing 2% BSA prepared in PBS for 30 min. Cells were given a single PBS wash and incubated with primary antibody (as per the dilution mentioned on the data sheet of the antibody) prepared in PBS and incubated at 4 °C for overnight. The next day, cells were washed thrice with PBS and incubated with FITC/TRITC/Cy3.5 conjugated secondary antibodies and

incubated for 2 h at 37 °C, followed by nuclear staining using Hoechst 33258 for 10 min. Cells were washed and visualized using a fluorescence microscope (Olympus IX83).

4.33. RNA extraction and quantitative reverse transcriptase-PCR (RT-qPCR)

dPC12 cells were treated with/without AOX and were used for RNA isolation. Total RNA was isolated from treated PC12 derived neurons using PureLink RNA Mini Kit (Cat. No. 12183018A, Invitrogen), following the manufacturer's protocol. The RNA concentration and purity ($A_{260}/A_{280} > 1.8$) of each sample were determined using the NanoDrop 1000 spectrophotometer (ThermoFisher Scientific). cDNA was synthesized using total RNA (300 ng) with RevertAid First Strand cDNA Synthesis Kit (Cat. No. K1621, Thermo Scientific) according to the manufacturer's instructions. The synthesized cDNA was then diluted 10 times with nuclease-free water for RT-qPCR. Reaction mix (10 μL) was prepared by adding 5 μL iTaqTM universal SYBR Green supermix (2 ×), 0.5 μL (10 μmol/L) of each specific primer pair, and 4 μL of diluted cDNA. The polymerase reaction was carried out using the standard fast protocol of 95 °C for 20 s for initial heating followed by 40 cycles of amplification that comprised of the following: 95 °C for 3 s and variable annealing temperature commencing from 57.2 to 58.2 °C for 30 s followed by 65 °C for 5 s. The expression levels of mRNA were normalized to GAPDH, used as an endogenous control. Primers listed in Table 1 were used for the amplification process and the relative mRNA expression was calculated using the $2^{-\Delta\Delta Ct}$ method.

4.34. Animal housing and care

Adult male Wistar rats (weighing 280−320 g) were used for the experiments and procured from Jai Narai Vyas University (JNVU), Jodhpur animal house facility. Animals were housed in polypropylene cages having aspen shavings bedding (NEPCO) and had free access to filtered water and food pellets (Purina 5L79) *ad libitum* under a 12/12 h light/dark cycle. The animal house was maintained at a constant temperature of 23 ± 2 °C and humidity of 55 ± 5%. All of the animals have been prior approved by the Institutional Animal Ethics Committee (UDZ/IAEC/Pr/2020/18). All experiments were performed by the Institutional Animal Ethics Committee (IAEC).

4.35. Experimental animals

Male Wistar rats, weighing 280−320 g, were randomly divided into three groups: Sham group (sham operation without tBCCAO surgery, $n = 9$); tBCCAO/R group (tBCCAO surgery (20 min occlusion) treated with 0.9% NaCl followed by 24 h reperfusion, $n = 9$); tBCCAO/R/AOX group (tBCCAO surgery (20 min occlusion) treated with 0.5 mg/kg AOX) followed by 24 h reperfusion, $n = 9$). The drugs were injected intraperitoneally at the time of reperfusion.

4.36. Transient bilateral common carotid artery occlusion (tBCCAO) model

Male Wistar rats were deeply anesthetized by intraperitoneal injection with ketamine (90 mg/kg) and xylazine (10 mg/kg) at a constant dose volume of 1 mL/kg body weight. After the toe pinch test for unconsciousness, they were fixed with adhesive tapes in the supine position on a heating pad (37 °C) for controlling the body temperature, and the mouth was inserted in the mask for constant oxygen supply. The neck of the animal was raised with the help of cotton bedding to facilitate visualization of the artery for occlusion. The neck area was shaved and disinfected with 70% alcohol. The right and left common carotid arteries were exposed through a midline incision on the neck. The common carotid arteries were occluded with mini-vascular clamps with a closing force of $150 \times g$ for 20 min. The vascular clamps were retracted and the wound was sutured, and the rats were kept in an incubation cage for recovery.

4.37. Neurological deficit scoring

After 24 h of reperfusion, all the animals were assessed for neurological deficits, according to the modified Neurological Severity Score (mNSS)[69]. Briefly, this method employs a scoring system where specific criteria are assigned with a numerical value, where a higher score indicates more severe deficits (scale: 0−18; normal score: 0; maximum deficit score: 18). The following were the criteria for scoring: Motor function (Score 0−6) = Limb flexion (0-normal resistance, 1-reduced resistance and 2-minimal resistance, limb symmetry (0-normal and 1-asymmetry), postural stability (0-maintains balance, 1-grasping and unsteady, 2-leaning to one side and 3-falling over); Sensory function (Score 0−2) = 0-normal sensory function and 2-severe impairment; Reflexes (Score 0−6) = 0-normal reflexes and 2-severely impaired.

4.38. Cerebral infarct volume assessment

After 24 h of reperfusion, 3 rats from each group were sacrificed by cervical dislocation, and the brains were harvested. The brain was then rinsed in PBS to remove excess blood and then was immersed in PBS and kept in a −20 freezer for 3 min to facilitate slicing of the brain. The brain was placed in the brain matrix and then five coronal sections of 2 mm thickness were sliced using a fine razor blade. The slices were collected in a Petri plate containing 0.05% TTC prepared in PBS for 30 min at 37 °C followed by fixation in 10% buffered formalin. Brain slices were photographed with a camera along with a ruler and analyzed by ImageJ analysis software. The % infarction size was calculated as Eq. (12):

$$\text{Infarction}\ (\%) = [\text{Brain slice area} - \text{Total infarct area}\ (\text{Cortex} + \text{Straitum})\,] \times 100 \tag{12}$$

4.39. Cardiac perfusion-fixation and tissue processing

Adult male Wistar rats were anesthetized after 24 h of reperfusion after tBCCAO surgery with intraperitoneal injection of a mixture of ketamine (90 mg/kg) and xylazine (10 mg/kg) at a constant dose volume of 1 mL/kg body weight using a 1 mL calibrated syringe and then were perfused transcardially with PBS and simultaneously fixed with 10% buffered formalin. After perfusion-fixation, the brain was dissected out and post-fixed in the same fixative for another 24 h. Then each brain was processed for paraffin blocking by dehydration in increasing gradation of

alcohol dilution, clearing in xylene and finally infiltration with paraffin solution followed by embedding in paraffin blocks. After the blocks were prepared, 5 μm thick coronal sections were obtained with a rotatory microtome (Thermo Scientific HM 325) and collected on poly-D-lysine coated glass slides.

4.40. Histopathological and immunohistochemical analysis

Standard hematoxylin−eosin staining was performed. Tissue slides were deparaffinized and incubated for 8 min in Mayer's hematoxylin solution and washed in warm water for 10 min sections were dipped in 95% ethanol and counterstained with eosin for 30 s. The slides were then dipped in xylene and mounted in DPX and visualized by Dewinter microscope.

For immunohistochemical analysis slides with brain sections were dried at 37 °C for 30 min for better adherence of the sections to avoid washing out. Paraffin was removed from the slides by dipping the slides in xylene, followed by rehydration in a gradation of decreasing alcohol dilution. Antigen retrieval was performed by using the microwave method as instructed for the antibody by the manufacturer. Briefly, for anti-S100β and anti-IBA1 Tris/EDTA solution and anti-GFAP sodium citrate solution was used to dip the slides and microwave at 700W till boiling followed by 20 min microwave at 140 W and rinsed thrice with PBS. Slides were permeabilized with 1% Triton-X 100 in PBS for 30 min at RT followed by rinsing with PBS 3 times. Endogenous peroxidase was blocked by incubating the slides with 1% hydrogen peroxide in PBS for 30 min at RT and blocked using 1% normal serum for 95 min. The sections were then incubated with primary antibodies raised against S100β (1:1000), IBA1(1:2000), and GFAP (1:500) diluted in 1% BSA in PBST at 4 °C for overnight in humidified condition. The next day, the slides were washed with PBST and incubated with fluorophore-conjugated secondary antibodies for 2 h in the dark at RT. The slides were washed with PBS and the nuclei were stained with DAPI and mounted in a HARDSET VECTOR mounting medium with an anti-fade agent. The slides were examined under a fluorescence microscope (OLUMPUS IX83) and the corrected total cell fluorescence (CTCF) intensities were quantified using ImageJ software and expressed in arbitrary units (A.U.), as shown in Eq. (13):

$$\begin{aligned}\text{CTCF} = {} & \text{Integrated density} - (\text{Area of selected cell} \\ & \times \text{Mean fluorescence of background readings})\end{aligned} \tag{13}$$

4.41. SHOLL and fractal analysis

To quantify the ramification of microglia of the cortex and striatum region, Sholl and fractal analysis was performed using a plugin for ImageJ software Sholl analysis and FracLac[70]. The brain sections immunolabeled for IBA1 were used to study the microglia. Single cells were extracted from the image, thresholded, and skeletonized to perform the analysis. Fractal analysis quantified the cell density, span ratio, and circularity data which described the size, elongation, and shape of the cell outline, respectively.

4.42. Statistical analysis

All of the results that were presented as the mean accompanied by the standard deviation (SD) were representative of at least three or four separate experiments. When comparing the mean values of more than two different groups, a one-way analysis of variance (ANOVA) was performed, on the data using Prism software (GraphPad Prism Software Inc., Version 8.0.2). A statistic was considered statistically significant if it had a *P*-value of less than 0.05.

Acknowledgments

Juhee Khan thanks INSPIRE for her fellowship, Prabir Kumar Gharai and S. Gupta thank CSIR; Shubham Garg thanks MHRD and IIT Jodhpur for fellowship. Mohammad Umar Arshi thank SERB, India for Project fellowship. Surajit Ghosh kindly acknowledges SERB, India (CRG/2019/000670, India) for financial support. Rathnam Mallesh thank IIT Jodhpur for infrastructure and fellowships. Surajit Ghosh also thanks JNVU, Jodhpur for animal experiments after receiving the approval for performing the animal experiments from the animal ethics committee. We wish to thank Prof. P. Jaisankar, CSIR-IICB for his kind and generous support. We thank CSIR-IICB Kolkata and IIT Jodhpur for providing infrastructure.

Author contributions

Juhee khan: Writing − review & editing, Writing − original draft, Visualization, Validation, Software, Resources, Project administration, Methodology, Investigation, Formal analysis, Data curation, Conceptualization. Prabir kumar Gharai: Writing − review & editing, Writing − original draft, Visualization, Validation, Software, Methodology, Formal analysis, Data curation, Conceptualization. Shubham Garg: Writing − review & editing, Writing − original draft, Visualization, Software, Formal analysis, Data curation. Sanju Gupta: Writing − review & editing, Writing − original draft, Visualization, Software, Methodology, Formal analysis, Data curation. Mohammad Umar Arshi: Writing − review & editing, Writing − original draft, Visualization, Methodology, Formal analysis, Data curation, Conceptualization. Rathnam Mallesh: Writing − original draft, Software, Formal analysis, Data curation, Conceptualization. Surajit Ghosh: Writing − review & editing, Writing − original draft, Visualization, Validation, Supervision, Software, Resources, Project administration, Methodology, Investigation, Funding acquisition, Formal analysis, Data curation, Conceptualization.

Conflicts of interest

The authors declare no conflicts of interest.

Appendix A. Supporting information

Supporting information to this article can be found online at https://doi.org/10.1016/j.apsb.2025.04.024.

References

1. Lamptey RNL, Chaulagain B, Trivedi R, Gothwal A, Layek B, Singh J. A review of the common neurodegenerative disorders: current therapeutic approaches and the potential role of nanotherapeutics. *Int J Mol Sci* 2022;**23**:1851.
2. Lin MT, Beal MF. Mitochondrial dysfunction and oxidative stress in neurodegenerative diseases. *Nature* 2006;**443**:787−95.
3. Rose J, Brian C, Woods J, Pappa A, Panayiotidis MI, Powers R, et al. Mitochondrial dysfunction in glial cells: implications for neuronal homeostasis and survival. *Toxicology* 2017;**391**:109−15.

4. Boveris A, Oshino N, Chance B. The cellular production of hydrogen peroxide. *Biochem J* 1972;**128**:617−30.
5. Holmström KM, Finkel T. Cellular mechanisms and physiological consequences of redox-dependent signalling. *Nat Rev Mol Cell Biol* 2014;**15**:411−21.
6. Murphy MP. How mitochondria produce reactive oxygen species. *Biochem J* 2009;**417**:1−13.
7. Chouchani ET, Pell VR, James AM, Work ML, Parsy SK, Frezza C, et al. A unifying mechanism for mitochondrial superoxide production during ischemia−reperfusion injury. *Cell Metab* 2016;**23**:254−63.
8. Niatsetskaya ZV, Sosunov SA, Matsiukevich D, Sosunova IVU, Ratner VI, Starkov AA, et al. The oxygen free radicals originating from mitochondrial complex I contribute to oxidative brain injury following hypoxia−ischemia in neonatal mice. *J Neurosci* 2012;**32**:3235−44.
9. Phaniendra A, Jestadi DB, Periyasamy L. Free radicals: properties, sources, targets, and their implication in various diseases. *Indian J Clin Biochem* 2015;**30**:11−26.
10. Pham-Huy LA, He H, Pham-Huy C. Free radicals, antioxidants in disease and health. *Int J Biomed Sci* 2008;**4**:89−96.
11. Di Meo S, Reed TT, Venditti P, Victor VM. Role of ROS and RNS sources in physiological and pathological conditions. *Oxid Med Cell Longev* 2016;**2016**:1245049.
12. Prachayasittikul V, Prachayasittikul S, Ruchirawat SPV. 8-Hydroxyquinolines: a review of their metal chelating properties and medicinal applications. *Drug Des Dev Ther* 2013;**7**:1157−78.
13. Mezzaroba L, Alfieri DF, Colado Simão AN, Vissoci Reiche EM. The role of zinc, copper, manganese and iron in neurodegenerative diseases. *Neurotoxicology* 2019;**74**:230−41.
14. Crichton RR, Dexter DTWR. Brain iron metabolism and its perturbation in neurological diseases. *J Neural Transm* 2011;**118**:301−14.
15. Tõugu V, Palumaa P. Coordination of zinc ions to the key proteins of neurodegenerative diseases: aβ, APP, α-synuclein and PrP. *Coord Chem Rev* 2012;**256**:2219−24.
16. Bush AI. The metallobiology of Alzheimer's disease. *Trends Neurosci* 2003;**26**:207−14.
17. Bush AI, Tanzi RE. Therapeutics for Alzheimer's disease based on the metal hypothesis. *Neurotherapeutics* 2008;**5**:421−32.
18. Gaeta A, Hider RC. The crucial role of metal ions in neurodegeneration: the basis for a promising therapeutic strategy. *Br J Pharmacol* 2005;**146**:1041−59.
19. Zatta P, Drago D, Bolognin S, Sensi SL. Alzheimer's disease, metal ions and metal homeostatic therapy. *Trends Pharmacol Sci* 2009;**30**: 346−55.
20. Perez LR, Franz KJ. Minding metals: tailoring multifunctional chelating agents for neurodegenerative disease. *Dalton Trans* 2010;**39**: 2177−87.
21. Mansouri MT, Farbood Y, Sameri MJ, Sarkaki A, Naghizadeh B, Rafeirad M. Neuroprotective effects of oral gallic acid against oxidative stress induced by 6-hydroxydopamine in rats. *Food Chem* 2013;**138**:1028−33.
22. Badhani B, Sharma N, Kakkar R. Gallic acid: a versatile antioxidant with promising therapeutic and industrial applications. *RSC Adv* 2015; **5**:27540−57.
23. Priscilla DH, Prince PSM. Cardioprotective effect of gallic acid on cardiac troponin-T, cardiac marker enzymes, lipid peroxidation products and antioxidants in experimentally induced myocardial infarction in Wistar rats. *Chem Biol Interact* 2009;**179**:118−24.
24. Patel SS, Goyal RK. Cardioprotective effects of gallic acid in diabetes-induced myocardial dysfunction in rats. *Pharmacogn Res* 2011;**3**: 239−45.
25. Rasool MK, Sabina EP, Ramya SR, Preety P, Patel S, Mandal N, et al. Hepatoprotective and antioxidant effects of gallic acid in paracetamol-induced liver damage in mice. *J Pharm Pharmacol* 2010;**62**:638−43.
26. Kroes BH, van den Berg AJ, Quarles van Ufford HC, van Dijk H, Labadie RP. Anti-inflammatory activity of gallic acid. *Planta Med* 1992;**58**:499−504.
27. Sun J, Li YZ, Ding YH, Wang J, Geng J, Yang H, et al. Neuroprotective effects of gallic acid against hypoxia/reoxygenation-induced mitochondrial dysfunctions *in vitro* and cerebral ischemia/reperfusion injury *in vivo*. *Brain Res* 2014;**1589**:126−39.
28. Kim MJ, Seong AR, Yoo JY, Jin CH, Lee YH, Kim YJ, et al. Gallic acid, a histone acetyltransferase inhibitor, suppresses β-amyloid neurotoxicity by inhibiting microglial-mediated neuroinflammation. *Mol Nutr Food Res* 2011;**55**:1798−808.
29. Yu M, Chen X, Liu J, Ma Q, Zhuo Z, Chen H, et al. Gallic acid disruption of Aβ(1−42) aggregation rescues cognitive decline of APP/PS1 double transgenic mouse. *Neurobiol Dis* 2019;**124**:67−80.
30. Guo S, Bezard E, Zhao B. Protective effect of green tea polyphenols on the SH-SY5Y cells against 6-OHDA induced apoptosis through ROS−NO pathway. *Free Radic Biol Med* 2005;**39**:682−95.
31. Weinreb O, Mandel S, Amit T, Youdim MBH. Neurological mechanisms of green tea polyphenols in Alzheimer's and Parkinson's diseases. *J Nutr Biochem* 2004;**15**:506−16.
32. Lim HJ, Shim SB, Jee SW, Lee SH, Lim CJ, Hong JT, et al. Green tea catechin leads to global improvement among Alzheimer's disease-related phenotypes in NSE/hAPP-C105 Tg mice. *J Nutr Biochem* 2013;**24**:1302−13.
33. More SV, Koppula S, Kim IS, Kumar H, Kim BW, Choi DK. The role of bioactive compounds on the promotion of neurite outgrowth. *Molecules* 2012;**17**:6728−53.
34. Fournier AE, Strittmatter SM. Repulsive factors and axon regeneration in the CNS. *Curr Opin Neurobiol* 2001;**11**:89−94.
35. McKerracher L. Spinal cord repair: strategies to promote axon regeneration. *Neurobiol Dis* 2001;**8**:11−8.
36. Reznichenko L, Amit T, Youdim MBH, Mandel S. Green tea polyphenol (−)-epigallocatechin-3-gallate induces neurorescue of long-term serum-deprived PC12 cells and promotes neurite outgrowth. *J Neurochem* 2005;**93**:1157−67.
37. Nagase H, Yamakuni T, Matsuzaki K, Maruyama Y, Kasahara J, Hinohara Y, et al. Mechanism of neurotrophic action of nobiletin in PC12D cells. *Biochemistry* 2005;**44**:13683−91.
38. Zhao S, Huang X, Whelton AJ, Abu-Omar MM. Renewable epoxy thermosets from fully lignin-derived triphenols. *ACS Sustain Chem Eng* 2018;**6**:7600−8.
39. Guggari S, Magliozzi F, Malburet S, Graillot A, Destarac M, Guerre M. Vanillin-based epoxy vitrimers: looking at the cystamine hardener from a different perspective. *ACS Sustain Chem Eng* 2023;**11**:6021−31.
40. Chang MY, Lin CY, Chen SM. Gram-scale synthesis of substituted triarylmethanes. *Synthesis* 2022;**54**:4561−75.
41. Hamley IW. The amyloid beta peptide: a chemist's perspective. Role in Alzheimer's and fibrillization. *Chem Rev* 2012;**112**:5147−92.
42. Kepp KP. Bioinorganic chemistry of Alzheimer's disease. *Chem Rev* 2012;**112**:5193−239.
43. Reybier K, Ayala S, Alies B, Rodrigues JV, Bustos Rodriguez S, La Penna G, et al. Free superoxide is an intermediate in the production of H_2O_2 by copper(I)−Aβ peptide and O_2. *Angew Chem Int Ed Engl* 2016;**55**:1085−9.
44. Barnham KJ, Bush AI. Biological metals and metal-targeting compounds in major neurodegenerative diseases. *Chem Soc Rev* 2014;**43**: 6727−49.
45. Jiang D, Zhang L, Grant GPG, Dudzik CG, Chen S, Patel S, et al. The elevated copper binding strength of amyloid-β aggregates allows the sequestration of copper from albumin: a pathway to accumulation of copper in senile plaques. *Biochemistry* 2013;**52**:547−56.
46. Kedare SB, Singh RP. Genesis and development of DPPH method of antioxidant assay. *J Food Sci Technol* 2011;**48**:412−22.
47. Chelliah R, Banan-MwineDaliri E, Oh DH. In: Dharumadurai D, editor. *Screening for antioxidant activity: nitric oxide scavenging assay BT—methods in actinobacteriology*. New York, NY: Springer US; 2022. p. 455−6.
48. Mesquita CS, Oliveira R, Bento F, Geraldo D, Rodrigues JV, Marcos JC. Simplified 2,4-dinitrophenylhydrazine spectrophotometric assay for quantification of carbonyls in oxidized proteins. *Anal Biochem* 2014;**458**:69−71.
49. Siddiqui MA, Kashyap MP, Kumar V, Tripathi VK, Khanna VK, Yadav S, et al. Differential protection of pre-, co- and post-treatment

of curcumin against hydrogen peroxide in PC12 cells. *Hum Exp Toxicol* 2011;**30**:192−8.
50. Shields HJ, Traa A, Van Raamsdonk JM. Beneficial and detrimental effects of reactive oxygen species on lifespan: a comprehensive review of comparative and experimental studies. *Front Cell Dev Biol* 2021;**9**: 628157.
51. Pradhan K, Das G, Gupta V, Mondal P, Barman S, Khan J, et al. Discovery of neuroregenerative peptoid from amphibian neuropeptide that inhibits amyloid-β toxicity and crosses blood−brain barrier. *ACS Chem Neurosci* 2019;**10**:1355−68.
52. Isayama K, Pitts LH, Nishimura MC. Evaluation of 2,3,5-triphenyltetrazolium chloride staining to delineate rat brain infarcts. *Stroke* 1991;**22**:1394−8.
53. Mittelbronn M, Dietz K, Schluesener HJ, Meyermann R. Local distribution of microglia in the normal adult human central nervous system differs by up to one order of magnitude. *Acta Neuropathol* 2001;**101**:249−55.
54. Lawson LJ, Perry VH, Gordon S. Turnover of resident microglia in the normal adult mouse brain. *Neuroscience* 1992;**48**:405−15.
55. Morrison H, Young K, Qureshi M, Rowe RK, Lifshitz J. Quantitative microglia analyses reveal diverse morphologic responses in the rat cortex after diffuse brain injury. *Sci Rep* 2017;**7**:13211.
56. Doorn KJ, Goudriaan A, Blits-Huizinga C, Bol JGJM, Rozemuller AJ, Hoogland PVJM, et al. Increased amoeboid microglial density in the olfactory bulb of Parkinson's and Alzheimer's patients. *Brain Pathol* 2014;**24**:152−65.
57. Heindl S, Gesierich B, Benakis C, Llovera G, Duering M, Liesz A. Automated morphological analysis of microglia after stroke. *Front Cell Neurosci* 2018;**12**:106.
58. Chen L, Yan C, Du BB, Wu K, Zhang LY, Yin SY, et al. Linear and nonlinear optical properties of Ln−Zn heteronuclear complexes from a Schiff base ligand containing 8-hydroxyquinoline moiety. *Inorg Chem Commun* 2014;**47**:13−6.
59. Wu MY, Esteban G, Brogi S, Shionoya M, Wang L, Campiani G, et al. Donepezil-like multifunctional agents: design, synthesis, molecular modeling and biological evaluation. *Eur J Med Chem* 2016;**121**:864−79.
60. Paizs C, Bartlewski-Hof U, Rétey J. Investigation of the mechanism of action of pyrogallol-phloroglucinol transhydroxylase by using putative intermediates. *Chemistry* 2007;**13**:2805−11.
61. Gharai PK, Khan J, Mallesh R, Garg S, Saha A, Ghosh S, et al. Vanillin benzothiazole derivative reduces cellular reactive oxygen species and detects amyloid fibrillar aggregates in Alzheimer's disease brain. *ACS Chem Neurosci* 2023;**14**:773−86.
62. Crescenzi O, Tomaselli S, Guerrini R, Salvadori S, D'Ursi AM, Temussi PA, et al. Solution structure of the Alzheimer amyloid beta-peptide (1−42) in an apolar microenvironment. Similarity with a virus fusion domain. *Eur J Biochem* 2002;**269**:5642−8.
63. Colvin MT, Silvers R, Ni QZ, Can TV, Sergeyev I, Rosay M, et al. Atomic resolution structure of monomorphic Aβ42 amyloid Fibrils. *J Am Chem Soc* 2016;**138**:9663−74.
64. Vijayan M, Bose C, Reddy PH. Anti-brain aging effects of small molecule inhibitor DDQ. *Mol Neurobiol* 2021;**58**:3588−600.
65. Ferrer P, Asensi M, Segarra R, Ortega A, Benlloch M, Obrador E, et al. Association between pterostilbene and quercetin inhibits metastatic activity of B16 melanoma. *Neoplasia* 2005;**7**:37−47.
66. Satyavert, Gupta S, Choudhury H, Jacob S, Nair AB, Dhanawat M, et al. Pharmacokinetics and tissue distribution of hydrazinocurcumin in rats. *Pharmacol Rep* 2021;**73**:1734−43.
67. Yan F, Yu X, Jing Y. Optimized preparation, characterization, and antioxidant activity of chitooligosaccharide-glycine Maillard reaction products. *J Food Sci Technol* 2018;**55**:712−20.
68. Wiemerslage L, Lee D. Quantification of mitochondrial morphology in neurites of dopaminergic neurons using multiple parameters. *J Neurosci Methods* 2016;**262**:56−65.
69. Chen J, Sanberg PR, Li Y, Wang L, Lu M, Willing AE, et al. Intravenous administration of human umbilical cord blood reduces behavioral deficits after stroke in rats. *Stroke* 2001;**32**: 2682−8.
70. Green TRF, Murphy SM, Rowe RK. Comparisons of quantitative approaches for assessing microglial morphology reveal inconsistencies, ecological fallacy, and a need for standardization. *Sci Rep* 2022;**12**:18196.